

UC Irvine

UC Irvine Electronic Theses and Dissertations

Title

Metalens-based Receiver Design for Free Space Optical Communication

Permalink

<https://escholarship.org/uc/item/65k7p0jr>

Author

Islam, Md Shafiqui

Publication Date

2024

Peer reviewed|Thesis/dissertation

UNIVERSITY OF CALIFORNIA,
IRVINE

Metalens-based Receiver Design for Free Space Optical Communication

DISSERTATION

submitted in partial satisfaction of the requirements
for the degree of

DOCTOR OF PHILOSOPHY

in Electrical and Computer Engineering

by

Md Shafiqul Islam

Dissertation Committee:
Professor Ozdal Boyraz, Chair
Associate Professor Hung Cao
Assistant Professor Hamidreza Aghasi

2024

Portion of Chapter 3 © 2023 Optica Publishing Group

Portion of Chapter 4 © 2023 Optica Publishing Group

All other materials © 2024 Md Shafiqul Islam

TABLE OF CONTENTS

	Page
LIST OF FIGURES	iv
LIST OF TABLES	vii
ACKNOWLEDGEMENTS	viii
VITA	ix
ABSTRACT OF THE DISSERTATION	x
CHAPTER 1: INTRODUCTION	1
CHAPTER 2: CHALLENGES OF FREE SPACE OPTICAL COMMUNICATION	8
CHAPTER 3: METASURFACE	12
3.1 Generalized Snell's Law	12
3.2 Generalized Snell's Law and Geometric Optics	15
3.3 Generalized Snell's Law in Cylindrical Coordinate System	17
3.4 Example of Phase-only Metasurface	18
3.5 Physical Design of Metasurface	20
3.6 Unit Cell Simulation	21
3.7 Full Wave Simulation of Metasurface	23
CHAPTER 4: AOA JITTER TOLERANT OPTICAL RECEIVER	26
4.1 Background	26
4.2 Proposed System	32
4.3 Result and Analysis	33
4.4 Full Wave Simulation	37
4.5 Region of Operation	41
CHAPTER 5: MULTI-BEAM COMMUNICATION SYSTEM	43
5.1 Background	43
5.2 Proposed System	44
5.3 Phase Profile of the First Metalens (ML1)	46
5.4 Phase Profile of the Second Metalens (ML2)	49
5.5 Result and Analysis	51
5.6 Meta Unit Cell	57
5.7 Full Wave Simulation of Multi-beam Receiver	58
CHAPTER 6: CONCLUSION	60

REFERENCES (OR BIBLIOGRAPHY) 62

APPENDIX A: Effect of Alignment in the AoA Jitter Tolerant Receiver 65

LIST OF FIGURES

	Page	
Figure 1.1	Two types of misalignment error in the FSO system	1
Figure 1.2	AoA variation from experimental measurement	2
Figure 1.3	Multibeam communication with conventional receiver	4
Figure 2.1	Block diagram of a typical FSO communication system	8
Figure 2.2a	Prototype of a satellite-based FSO system	10
Figure 2.2b	Block diagram of PAT system	10
Figure 2.3	Variation of E[BER] with jitter variance for the system	11
Figure 3.1	Ray diagram for deducing the Generalized Snell's Law	13
Figure 3.2a	Spherical wave from the individual unit cell	14
Figure 3.2b	Spherical waves from a collection of unit cells.	14
Figure 3.3	Ray propagation in the cylindrical coordinate system	17
Figure 3.4	Meta unit cell simulation layout	21
Figure 3.5	Transmission magnitude and phase variations of normally incident beam on meta unit cell structure with the diameter of the unit cell	22
Figure 3.6a	Quasi-3D simulation schematic in $u_2 - z$ plane	25
Figure 3.6b	Quasi-3D simulation schematic in $u_1 - z$ plane	25
Figure 4.1a	Conventional receiver with normal and oblique incident beam	26
Figure 4.1b	Beam walk-off on detector plane in the conventional receiver for normal and oblique incident beam	26
Figure 4.2a	Detector and beam overlap area (grey shaded region) for calculation of power degradation factor	28

Figure 4.2b	K versus beam walk-off (δ) for an ideal system with a detector radius of $20\mu m$	28
Figure 4.3a	BER for an ideal conventional system with a detector radius of $20\mu m$	30
Figure 4.3b	Power penalty for an ideal conventional system with a detector radius of $20\mu m$	30
Figure 4.4a	Proposed receiver with the normal and oblique incident beam	32
Figure 4.4b	Beam walk-off on detector plane in the proposed receiver for normal and oblique incident beam	32
Figure 4.5a	Ray diagram for the conventional receiver	34
Figure 4.5b	Ray diagram for the proposed receiver	34
Figure 4.6	Beam walk-off (δ) for different AoA (θ_{inc})	34
Figure 4.7a	Power degradation factor (K) for the conventional and the proposed receiver with detector radius $20\mu m$	36
Figure 4.7b	Power penalty for the conventional and the proposed receiver with detector radius $20\mu m$	36
Figure 4.7c	BER for the conventional and the proposed receiver with detector radius $20\mu m$	36
Figure 4.7d	E[BER] for different jitter variance	36
Figure 4.8	Simulation block diagram	38
Figure 4.9	Beam profile from POP calculation	39
Figure 4.10a	Fourier propagation result for $\theta_{inc} = 0$	40
Figure 4.10b	Fourier propagation result for $\theta_{inc} = 0.5mrad$	40
Figure 4.10c	Fourier propagation result for $\theta_{inc} = 0.5mrad$	40
Figure 4.11a	Beam walk-off, δ with different θ/θ_{opt}	42

Figure 4.11b	Performance degradation factor, K with different θ/θ_{opt}	42
Figure 4.11c	The region of operation for different θ_{opt} based on $K_{tol} = 0.5$ criteria	42
Figure 5.1	Variation of K in a conventional receiver system	43
Figure 5.2.	Proposed multi-beam receiver architecture	46
Figure 5.3	Coordinate system for incoming beam on ML1 and focused beam by ML1	49
Figure 5.4a	Ray diagram of the proof-of-concept system in the x-z plane	52
Figure 5.4b	Ray diagram of the proof-of-concept system in the y-z plane	52
Figure 5.5	Intensity profile on the detector for $m=1/10$	53
Figure 5.6	Variation of K with detector diameter D_i	54
Figure 5.7a	Ray diagram for multi-beam optical receiver system	55
Figure 5.7b	Performance factor for multi-beam optical receiver system	55
Figure 5.8	Variation of K for the proof-of-concept multi-beam system	56
Figure 5.9	Response of optimized meta-unit cell at wavelength $1.55\mu\text{m}$	57
Figure 5.10	FDTD simulation result of optical beam on the detector plane for different AoA	58
Figure 5.11	A pictorial representation of $R_{0.5}$ (--) with beam center (+) for $AoA = 0^\circ$ (blue), 1° (red), 2° (purple), and 3° (green)	59

LIST OF TABLES

		Page
Table 2.1	Optimized meta-unit cell parameters at the wavelength of $1\mu\text{m}$	22
Table 5.1	System parameters for an exemplary system	46
Table 5.2	Optimized meta-unit cell parameters at the wavelength of $1.55\mu\text{m}$	52

ACKNOWLEDGEMENTS

I would like to express my deepest appreciation to my committee chair, Professor Ozdal Boyraz. He always motivated me for deeper research and kept his confidence in me in times of failure. Without his guidance and persistent help, this dissertation would not have been possible.

I would like to thank my committee members, Professor Hung Cao and Professor Hamidreza Aghasi, whose research works always inspire me. Their valuable feedback helped improve my work and this dissertation.

I am also grateful to all the members of the APDSL research group, whose support helped me glide through the difficult times of my Ph.D.

A portion of Chapters 3 and 4 of this dissertation is a reprint of the material as it appears in [33], used with permission from the Optica Publishing Group. I would like to thank Kaveh Shahverdi and Ozdal Boyraz who is the co-authors of the publication.

Finally, I would like to express my gratitude to my parents, my wife, and my kid. Without their tremendous understanding and encouragement over the past few years, it would have been impossible for me to complete my studies.

VITA

Md Shafiqul Islam

2015	B.Sc. in Electrical and Electronic Engineering, Bangladesh University of Engineering and Technology, Dhaka, Bangladesh
2017-18	Graduate Student Fellowship, University of California, Irvine
2018-23	Graduate Student Researcher, University of California, Irvine
2021	M.Sc. in Electrical and Computer Engineering, University of California, Irvine
2024	Ph.D. in Electrical and Computer Engineering, University of California, Irvine

FIELD OF STUDY

Optical and Photonic System

PUBLICATIONS

- **Md Shafiqul Islam**, Ozdal Boyraz, "Metalens optical receiver for multi-beam free space optical communication " (under review)
- **Md Shafiqul Islam**, Ozdal Boyraz, "Wide field of regard metalens receiver for free space optical communication," Proc. SPIE 12666, Current Developments in Lens Design and Optical Engineering XXIV, 1266602 (2 October 2023); <https://doi.org/10.1117/12.2681775>
- **Md Shafiqul Islam**, Kaveh Shahverdi, and Ozdal Boyraz, "Metalens integrated receiver to reduce the effect of angle of arrival jitter in free space optical communication," J. Opt. Soc. Am. B 40, 891-899 (2023)
- **Md Shafiqul Islam** and Ozdal Boyraz, "Large Aperture and Wide Field of View Meta-Receiver for Free Space Optical Communications," in *Conference on Lasers and Electro-Optics*, Technical Digest Series (Optica Publishing Group, 2022)
- **Md Shafiqul Islam**, Imam-Uz Zaman, Parinaz Sadri-Moshkenani, Mohammad Wahiduzzaman Khan, Ozdal Boyraz, "Metalens wide-angle receiver for free space optical communications," Proc. SPIE 11814, Current Developments in Lens Design and Optical Engineering XXII, 1181409 (1 August 2021); <https://doi.org/10.1117/12.2596325>

ABSTRACT OF THE DISSERTATION

Metalens-based Receiver Design for Free-space Optical Communication

by

Md Shafiqul Islam

Doctor of Philosophy in Electrical and Computer Engineering

University of California, Irvine, 2023

Professor Ozdal Boyraz, Chair

Free space optical (FSO) communication has long been considered a promising solution for high-speed broadband data transfer. A conventional FSO receiver consisting of a focusing lens and a small high-speed detector works efficiently for a limited range of angles of arrival (AoA). This makes the optical link vulnerable to AoA fluctuations jitter. Even with a dedicated Pointing, Acquisition, and Tracking (PAT) system, residual jitter with variance in the range of microradian is unavoidable in FSO communication. The jitter causes BER fluctuations over a long time. Moreover, multi-beam optical communication in which one receiver needs to connect with multiple transmitters dispersed in 3D space at the same time cannot be implemented with the conventional receiver. This thesis presents two receiver designs based on metalenses that can offer solutions for these problems. To reduce the AoA fluctuation, a metalens is introduced at the focal plane of the bulk aperture lens of a conventional receiver. The phase profile of the lens is optimized to allow efficient capture of beams with AoAs as large as 2.5mrad. This is a significant improvement over a conventional receiver without metalens, which can capture only 195 μ rad with the same efficiency. For multi-beam communication, a two-metalens receiver system with optimized phase profiles

is proposed. A proof-of-concept three-beam communication link is demonstrated in which the maximum AoA of 2° can be captured with 67% efficiency. This shows 35X improvement over conventional systems with a single detector in terms of acceptable AoA. The performances of the proposed receivers are analyzed with diffractive optics calculation. Metalens unit cells at two different wavelengths ($1\mu\text{m}$ and $1.55\mu\text{m}$) are presented in this thesis. Full metalens systems are created based on the phase response of unit cells with varying diameters and simulated in Lumerical and COSMSOL. The simulation result validates the efficiency of the proposed receivers. When implemented, the proposed receiver will increase the capacity of communication links as well as maintain the same capacity over a long period of time. The proposed method can further be used to design receiver modules for specific situations such as for CubeSat/ astrophysical observation.

CHAPTER 1

INTRODUCTION

Free space optical (FSO) communication has recently regained its momentum because of emerging applications such as satellite-to-satellite communications, rapid rural area deployment, and data centers. It inherently provides high bandwidth, ease of deployment, license-free spectrum, low power consumption, and better channel security [1]. FSO links use an optical/near IR carrier to transmit data over an unguided medium [2]. Due to the small wavelength, carrier beam divergence is very small. As a result, FSO is a strict Line of Sight (LOS) system. The FSO link requires precise alignment between the transmitter and receiver. Misalignments lead to beam wandering on the receiver plane and detector plane. Beam wandering on the receiver aperture leads to pointing errors whereas beam wandering on the detector plane causes angle of arrival (AoA) deviation [3] both cause performance degradation of the communication link. The two types of error are shown in Figure 1.1.

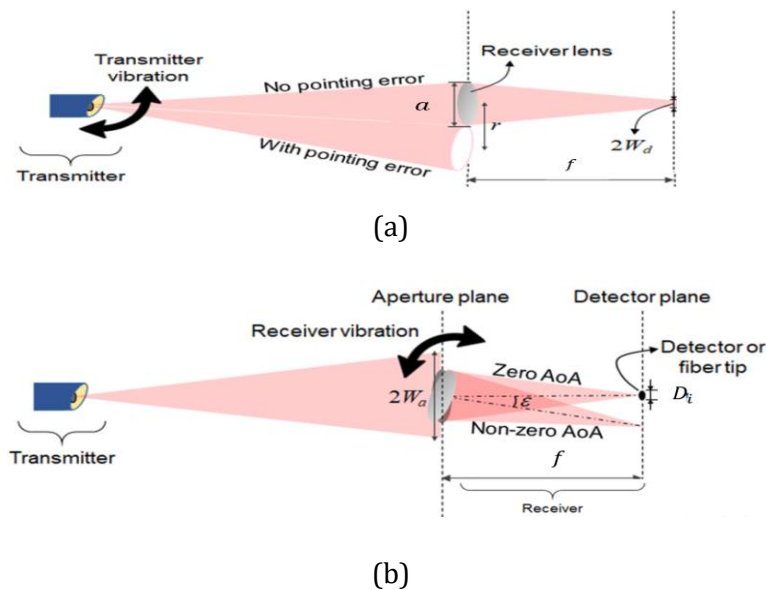


Figure 1.1 Two types of misalignment error in the FSO system (a) Pointing error (b) AoA deviation [3]

Pointing error is caused by transmitter vibration and turbulence in the propagating medium. The effect of pointing errors on the performance of the FSO system has been analyzed in numerous studies [4–6]. The impact of pointing error can be reduced by optimizing the transmitting beam waist in either a static [7] or dynamic [8] way.

A typical high-speed FSO link uses a small photodetector that provides high electrical bandwidth and reduces the effect of ambient light [9]. A large aperture lens is then used to collect and focus optical power on the detector. Due to the small detector size, the FSO receiver accepts light within a limited range of AoA. Even when the transmitter is fully illuminated (i.e., there is no pointing error), non-zero AoA causes the beam to wander on the detector plane and causes serious performance degradation of the communication link [9]. AoA deviation results from the vibration in the receiver module. Typically, deep space FSO receiver uses a dedicated Pointing, Acquisition, and Tracking (PAT) system to keep the receivers aligned with transmitters for data transfer. Even with PAT, some residual vibration is always present and AoA fluctuates randomly. A sample measurement data is shown in Figure 1.2.

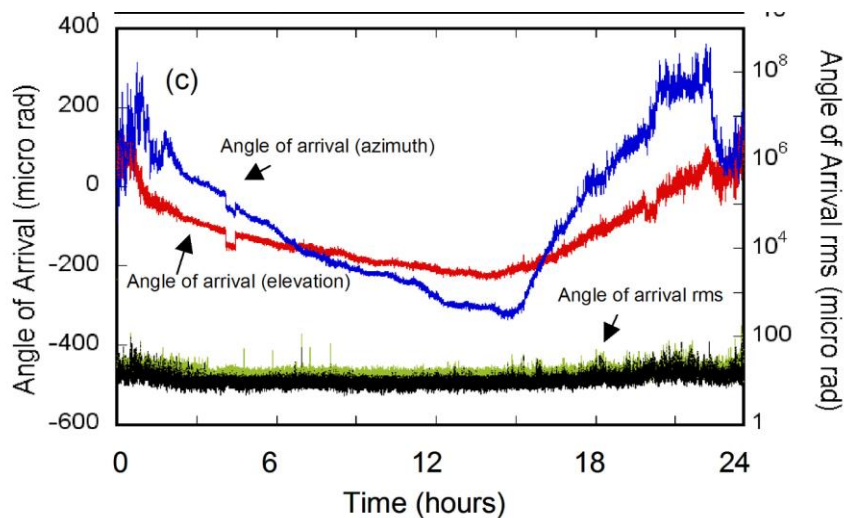


Figure 1.2. AoA variation from experimental measurement [10]

To date, several active control systems have been proposed to mitigate fluctuations in AoA and minimize performance degradation [10,11]. Such active control systems require additional processing power and mechanical control that put stress on the Size, Weight, and Power (SWAP) constraints of FSO communication. Adaptive beam size control by using an electrically tunable focusing lens is proposed [3]. Although the system eliminates the mechanical components, the system still requires additional processing to dynamically reduce the AoA fluctuation. In all these systems, due to slow response time and noise in the control systems, there is always a fast residual jitter in AOA, which significantly affects the Bit Error Rate (BER) of the system [12].

In this dissertation, we will propose a metalens-integrated receiver system that provides robust performance in the presence of the AoA jitter in the FSO link. The system performance degrades when the AoA deviates from the perfect alignment position, and hence the beam walks off on the detector plane. To maintain BER in the same way as normal incidence, the system must pay a power penalty. For instance, a beam walk-off of $19.5\mu\text{m}$ leads to a 3dB power penalty in a typical conventional FSO system using an $f/10$ aperture lens followed by a detector with a $20\mu\text{m}$ radius. In other words, the system with a 100mm focal length tolerates up to $195\mu\text{rad}$ AOA deviation with a 3dB power penalty. Here we will show that the FSO receiver with metalens maintains the same BER up to 2.5mrad AoA deviation with less than 3dB power penalty. The proposed metalens is based on a meta-unit cell, which consists of a-Si nanopillar on a quartz substrate. Full 2π phase shift with more than 93% transmission is achievable by varying the nanopillar diameter at the desired target wavelength. Here, we show how the metalens phase profile is optimized by using the receiver lens model available in commercial ray-tracing software and according to the

location of the metalens in a conventional receiver system at a wavelength of $1\mu\text{m}$. Considering the efficiency and ease of fabrication, the proposed design can be tailored to other metasurfaces with optimized phase profiles. Since the system is static, free of mechanical parts, and requires no active control mechanisms, it provides a simple and easy-to-implement solution to reduce the effect of jitter on the FSO system performance. Also, further optimizations are possible for different aperture lenses to accommodate higher AOA variations.

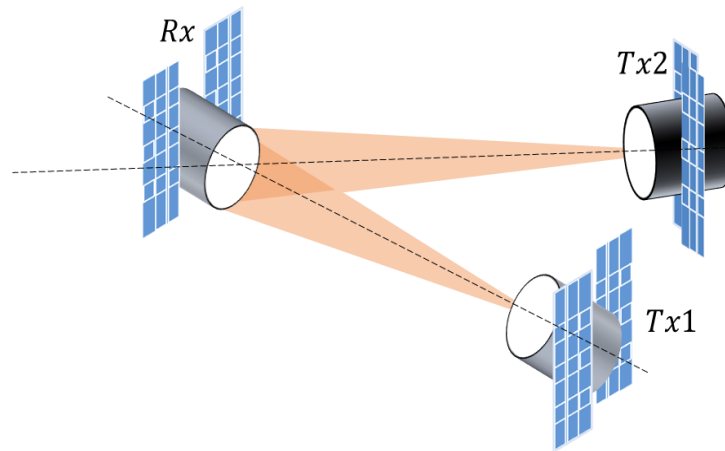


Figure 1.3. Multi-beam communication with conventional receiver

A limited field of regard of an FSO receiver implies that a receiver can only communicate with a single transmitter at a time. For example, in Figure 1.3, the receiver aperture is fully illuminated by the two incoming optical beams from two transmitters, Tx1 and Tx2. However, only the incoming beam from Tx1 with zero AoA can establish effective communication. Thus, the FSO receiver allows only point-to-point communication between a single transmitter and receiver pair. Multi-beam communication using multiple transmitters can improve FSO communication through diversity and multiplexing [13]. Spatial diversity helps to overcome the limit of optical power and introduces redundancy to

combat the fading effect of turbulent optical channels [14]. On the other hand, multiplexing increases the overall capacity of the FSO link. Typically, a receiver with a detector array is used for multi-beam communication. In such a system, one needs to consider additional detector noise [15]. The detector array also makes the system bulky, which is detrimental to airborne FSO communication links.

In the second part of the dissertation, we will propose a single-point detector receiver system that can capture optical beams coming with different AoAs to enable communication with multiple nodes dispersed in space. The proposed systems consist of two metalenses with customized phase profiles. We propose a metalens design with a 2D phase profile to facilitate the focusing of the incoming beam on both transverse dimensions (like spherical lenses). For this system, we will provide a detailed description of phase profiles for the proposed two metalenses. The performance of the proof-of-concept system is analyzed with the proposed phase profiles. Finally, we will demonstrate a 3D full receiver system simulation using the FDTD method. The proposed approach improves detection efficiency for optical beams coming from non-zero arbitrary AoAs in 3D space.

The proof of concept has been evaluated using a three-beam optical link and our proposed single-detector optical receiver. Here, we assume that each beam is separated by 1° in space, where one of the links is perfectly aligned with the receiver's optical axis. In conventional systems, the AoA variation of 2° leads to 1.7mm beam walk-off and necessitates a detector array to capture such 2° variations in the incidence angle. We show that our proposed metalens design reduces the beam walk-off to $2.61\mu\text{m}$. Our system also focuses all the beams with different AoAs to the same point detectors, leading to high detection efficiency. For example, an off-axis beam with 2° AoA can be captured with 70%

detection efficiency by a detector diameter of $100\mu\text{m}$ by using diffraction optics simulations. Conventional systems using a single focusing lens can capture only 0.056° with the same detection efficiency. Thus, our system shows 35 times improvement over the conventional system regarding the acceptable AoA. A 3D FDTD simulation also verifies that an off-axis beam with 2° AoA can be captured with about 67% detection efficiency by a point detector. The proposed system is scalable to accept larger AoA variations to enable the detection of data emitted by spatially dispersed transmitters. Since our system will eliminate the need for bulk aspheric lenses, it will work within the Size, Weight, and Power (SWAP) constraints of satellite-based free space optical communication.

The use of metasurfaces in electromagnetics and photonics was proposed five decades ago. Metasurfaces have emerged as a promising technology for wavefront shaping in optics due to their various useful properties such as monolithic integration, compact design, and subwavelength control [16]. Metasurfaces have found applications in diffraction-limited focusing and imaging [17,18], polarization control [19], holography [20], and AR/VR systems [21]. For imaging, wide field of view (WFOV) metalens have been proposed in [22,23]. In these systems, optical beams with different incident angles get focused on different locations on the detector plane, and hence a detector array captures light for all incident angles. Mostly, such systems are designed for CMOS image sensors [24]. Since a single point detector is used in communication systems, the metalens design criteria for FSO receivers differ from imaging systems that have been studied before. This dissertation provides design guidelines for metalenses to be used in the FSO system.

Currently, optical fiber serves as the backbone for high-speed data communication. Fiber optic communication can reach beyond 1Tb/s capacity by using Dense Wavelength

Division Multiplexing (DWDM) [10] . However, with the increasing demand for broadband wireless data transfer, communication using free-space optical (FSO) systems has recently gained more attention. Existing receiver architecture with conventional lens suffers from AoA instability and inability to multi-beam communication, which prevents FSO from reaching its full potential. The proposed systems presented in this dissertation will solve these problems.

CHAPTER 2

CHALLENGES OF FREE SPACE OPTICAL COMMUNICATION

Free space optical (FSO) communication uses carrier signals from visible to near-infrared wavelengths. Due to high carrier frequency ($\approx 10^{16} \text{ Hz}$), FSO offers a high signal bandwidth which is almost 10^5 times that of a typical RF carrier [1]. It enables high-rate data communication between two fixed points. The block diagram of a typical FSO communication is shown in Figure 2.1.

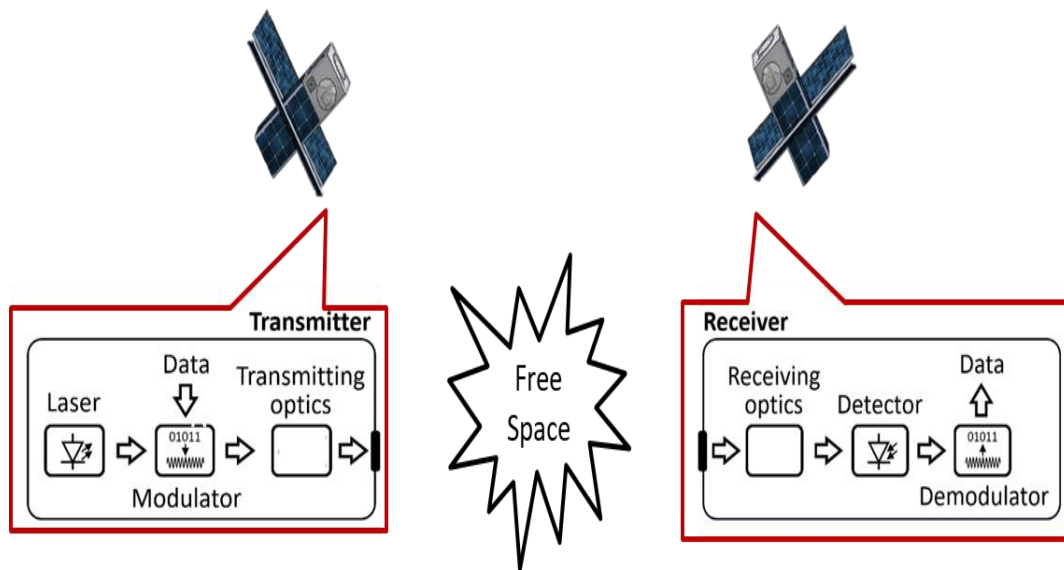


Figure 2.1. Block diagram of a typical FSO communication system

FSO transmitter uses a laser as the source. Data is encoded on the laser output power in intensity modulation communication format. The divergent beam from the laser chip is collimated by transmitting optics. The collimated optical beam propagates through the free space and reaches the optical receiver on the other end. The receiving optics focus the captured power on its aperture to the photodetector. After demodulation, the original data is decoded using decision circuitry.

Several factors affect the power reaching the detector from the transmitter. Some of the major losses in the FSO system are as follows.

1. Geometric loss
2. Absorption loss in the propagating medium (such as atmospheric loss)
3. Scattering and turbulence in the propagating medium
4. Pointing error
5. Angle of arrival deviation
6. Component loss

Geometric loss (L_G) refers to the loss due to only the divergence of the optical beam when propagating through the unguided medium. It depends on the transmitting beam's divergence (θ_{div}), link distance (d_L), and the receiver lens aperture diameter (D_R). In general, the relationship can be written as

$$L_G \propto \frac{D_R^2}{d_L^2 \theta_{div}^2} \quad (2.1)$$

The proportionality constant depends on the specific beam's intensity distribution and its evolution in free space.

Losses (L_M) due to absorption, scattering, and turbulence impact the performance of terrestrial FSO links. Space-based FSO links do not suffer from these losses. Component loss (L_C) arises from different components used in FSO transceivers such as angle-dependent detector responsivity η_λ , reflection due to Anti-Reflection (AR) coating η_{AR} , and free space to collimating and focusing Lens (FL) coupling efficiencies (η_C and η_F) [12] etc.

Both terrestrial and space based FSO links suffer from loss (L_P) due to pointing error. Pointing error arises when the axis of the transmitting beam does not go through the center of the receiver aperture. As a result, the receiver aperture lens cannot capture the full power available at the aperture plane. Including these losses the power captured by the receiver aperture can be written as

$$P_{rec} = P_T L_G L_M L_C L_P \quad (2.2)$$

Here, P_T is the power transmitted from the source.

This thesis particularly focuses on the loss (L_A) due to the angle of arrival (AoA) deviation error. AoA deviation occurs when the receiver's optical axis is not aligned with the transmitting beam's optical axis. This can arise due to the vibration in the receiver modules or waveform tilt from the turbulence. L_A depends on the detector diameter and the receiving optics. AoA deviation causes further degradation of power captured by the photodetector (P_d).

$$P_d = P_{rec} L_A \quad (2.3)$$

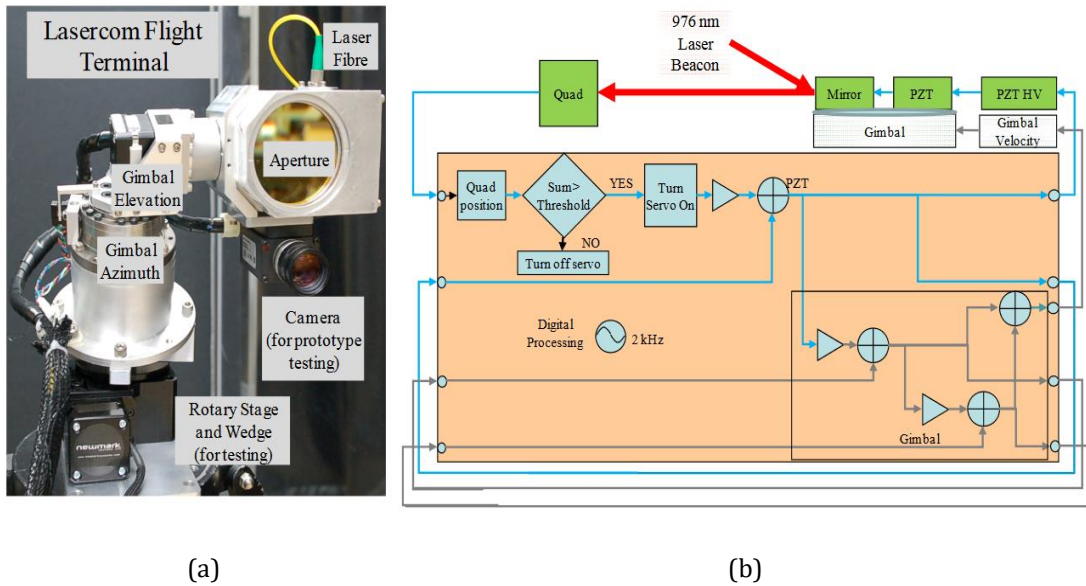


Figure 2.2. (a) Prototype of a satellite-based FSO system, (b) block diagram of PAT system [25]

A complex PAT system is implemented in a satellite-based FSO system to keep the pointing error and AoA deviation error at a minimum level. The prototype of such a system with the PAT used in [25] is shown in Figure 2.2a and the block diagram of the PAT system is shown in Figure 2.2b. The PAT system uses a quad-detector for tracking beam movement on the receiver plane. The feedback signal actuates gimbal motors to keep the receiver pointing towards the right direction. Due to noise and the limited speed of the feedback system, some residual jitter is always present in the system. Moreover, additional mechanical movements interfere with the satellite's altitude control system.

Even with the PAT system, AoA varies randomly in time. The fluctuations jitter cause Bit Error Rate (BER) fluctuation of the FSO link. The statistical average of AoA is one of the crucial parameters of the FSO link. The average depends on the receiver architecture. For example, the variation of average BER for a receiver with compressing telescope architecture is analyzed [26].

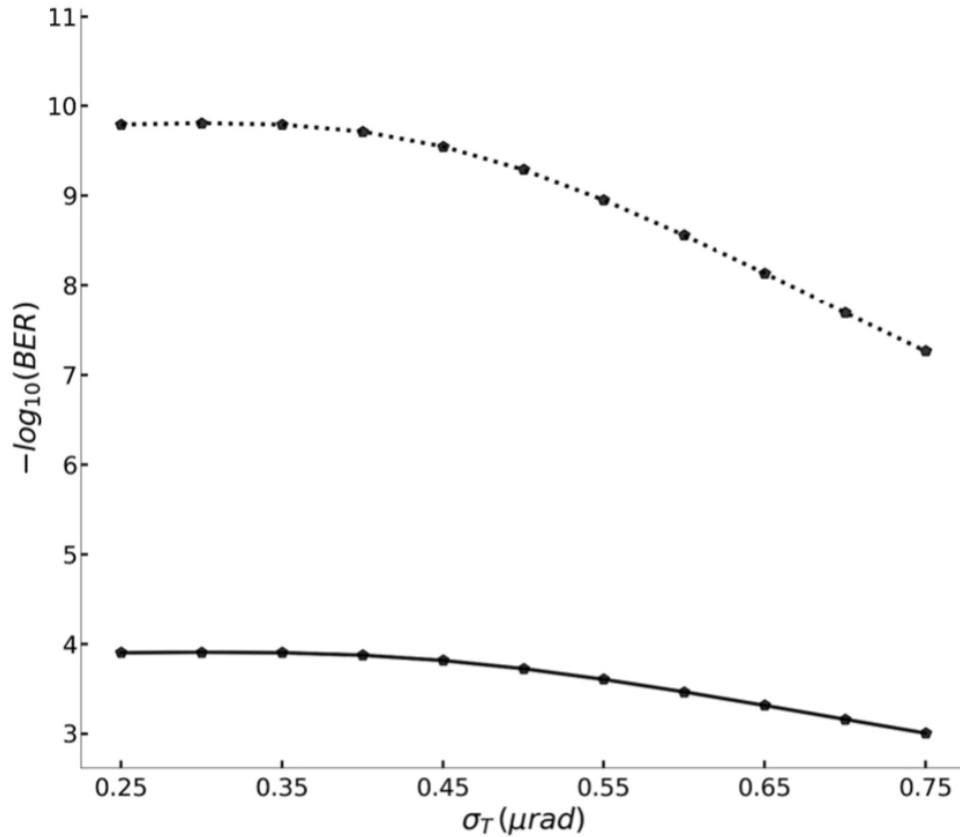


Figure 2.3. Variation of $E[\text{BER}]$ with jitter variance for the system with f - number = 2 (solid curve) and f - number = 3 (dashed curve) [25]

Figure 2.3 shows that a high f-number makes the system less susceptible to jitter variances. However, the BER is lower compared to the BER of a lower f-number system for the same jitter variance. We performed a similar analysis for much simplified receiving optics and arrived at the same conclusion which will be presented in Chapter 4.

CHAPTER 3

METASURFACE

Metasurfaces are built with subwavelength structures that can introduce abrupt changes in the properties of electromagnetic radiation and optical beams. These changes can be a combination of amplitude, phase, and polarization of the incident radiation. Such systems have been heavily utilized in antenna systems....., [27,28], in communication systems to create smart surfaces to combat fading and multi-path interferences [29], and in optics to create orbital angular momentum beams..... [30].

In optics, phase-only metasurfaces are more common and are used to build flat lenses and beam deflectors. These types of metasurfaces work based on the Generalized Snell's Law [31].

3.1 Generalized Snell's Law

Light reflects and refracts from the interface of two dissimilar materials. According to Snell's Law, the angle of reflection is equal to the angle of incidence. Also, the sine of the angle of refraction multiplied by the refractive index of the transmitting medium is equal to the sine of the angle of incidence multiplied by the refractive index of the incident medium. But this is applicable when there is no phase gradient on the interface. If a phase gradient is present on the interface, Generalized Snell's Law is applicable. One can prove Generalized Snell's Law by using Fermat's principle. Fermat's principle states that the path taken by a ray between two given points is the path that can be traveled in the least time or least phase change for monochromatic light.

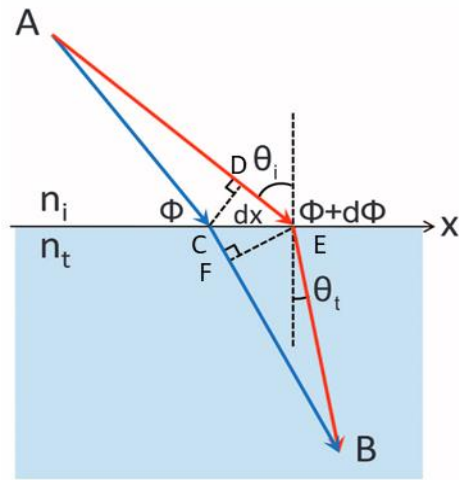


Figure 3.1. Ray diagram for deducing the Generalized Snell's Law [31]

Consider light is traveling from point A to point B. Two ray paths are drawn which are separated by a distance dx on the interface between the two media where $dx \rightarrow 0$. The phase difference (dP) between the two ray paths can be calculated as follows.

$$dP = n_i k_0 (AE - AC) + n_t k_0 (EB - CB) + d\Phi \quad (3.1)$$

From Figure 3.1.,

$$\begin{aligned} AC &= \sqrt{AE^2 - 2 AE dx \sin\theta_i + dx^2} \\ &= AE \sqrt{1 - 2 \frac{dx}{AE} \sin\theta_i + \frac{dx^2}{AE^2}} \\ &\approx AE - dx \sin\theta_i \end{aligned}$$

Here, we ignored second and higher-order terms. By a similar method, we can show that

$$CB \approx EB + dx \sin\theta_t$$

From Eq. 1,

$$dP = \left[k_0 (n_i \sin\theta_i - n_t \sin\theta_t) + \frac{d\Phi}{dx} \right] dx$$

The red path will be allowed optical path given that $dP = 0$ for any dx . This is true if

$$k_0 (n_t \sin\theta_t - n_i \sin\theta_i) = \frac{d\Phi}{dx} \quad (3.2)$$

Now, Eq. (3.2) represents Generalized Snell's Law. For zero phase gradient ($\frac{d\Phi}{dx} = 0$), it gives the equation for ordinary Snell's Law. Metasurface uses subwavelength structures which are separated in space by small but non-zero distances Δx . Usually, $\Delta x < \lambda$. This creates discrete phase gradients ($\frac{\Delta\Phi}{\Delta x}$). The subwavelength structure is called a unit cell. We can deduce a similar result as Eq. (3.2) by considering the overall response as the sum of the response of individual meta-unit cells.

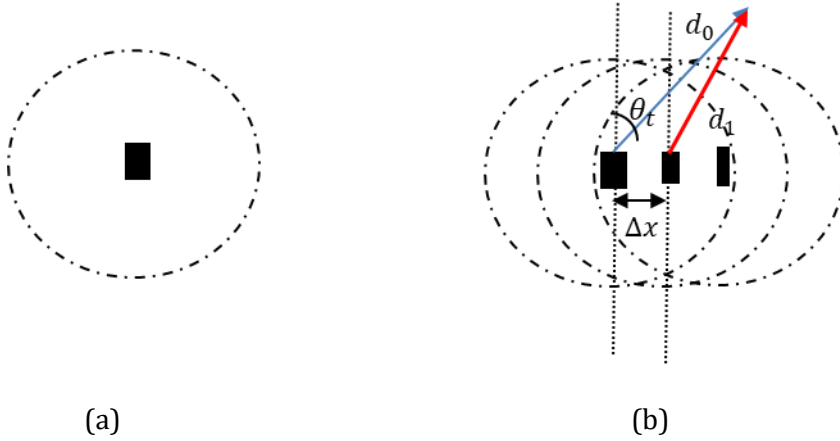


Figure 3.2. Spherical wave from the individual unit cell (a), interference of spherical waves from the collection of unit cells (b).

Assume, the unit cells are separated by Δx . We are observing their response in the far field ($d_0, d_1 \gg \lambda$), which can easily be justified in real-life scenarios as both the dimension of the unit cell and separation are smaller than the wavelength of light. The unit cell creates a far-field response $E_U e^{jk_0 d + j\Phi_U}$ which is proportional to the input field E_{in} . E_U and Φ_U vary with the unit cell's physical dimension (such as diameter). From Figure 3.2 we can write

$$d_n \approx d_0 - n\Delta x \sin\theta_t \text{ and } \theta_{tn} \approx \theta_t$$

The total field is the sum of the field from individual unit cells.

$$E_{tot} = E_U e^{jk_0 d_0} \sum e^{-jk_0 n \Delta x \sin \theta_t + j \Phi_U(n \Delta x)}$$

Constructive interference occurs when the following condition is satisfied.

$$-k_0 \sin \theta_t + \frac{\Delta \Phi_U}{\Delta x} = m 2\pi$$

With an oblique incident beam on the metasurface plane, we get

$$k_0 (\sin \theta_t - \sin \theta_i) = m 2\pi + \frac{\Delta \Phi}{\Delta x}$$

As $\Delta x < \lambda$, only $m = 0$ gives the propagating solution, i.e.

$$k_0 (\sin \theta_t - \sin \theta_i) = \frac{\Delta \Phi}{\Delta x}$$

Again, we obtain the equation same as Eq. (3.2).

3.2 Generalized Snell's Law and Geometric Optics

In three dimensions, Generalized Snell's Law can be written as

$$\vec{k}_{tr}^{out} - \vec{k}_{tr}^{in} = \nabla \Phi$$

Here, $\vec{k}_{tr}^{out}(\vec{k}_{tr}^{in})$ is the transverse/in-plane wavevector component of the output (input) wavevector. The out-of-plane wavevector component (k_z) is related to the in-plane component as $k_{tr}^2 + k_z^2 = k_0^2$. The overall wavevector is $\vec{k} = \vec{k}_{tr} + k_z \hat{z}$.

In geometric optics, light beams are considered as the collection of optical rays. Each ray has an origin (\vec{S}_0) and a propagation direction which is the same as the direction of the wavevector \vec{k} at \vec{S}_0 . In free space, the ray propagates in a straight line. The endpoint (\vec{S}_e) of the ray is calculated from \vec{S}_0 and \vec{k} as $\vec{S}_e = \vec{S}_0 + l \frac{\vec{k}}{|\vec{k}|}$, where l is the length of the ray in free space and $|\vec{k}| = nk_0$ is free space wavenumber in transmitting medium with refractive index

n . When the ray meets a boundary between two mediums, ordinary Snell's Law ($\nabla\Phi = 0$) is applied to find the ray propagation direction in the transmitting medium. The analysis is continued until the ray hits the detector/ image surface. The output beam profile or image is created by the intercepts of all the propagated rays on the detector/image surface. The analysis can be easily extended for the case $\nabla\Phi \neq 0$. This way, we can carry out a functional simulation of the metasurface.

In metasurface analysis, the origins (\vec{S}_0) and incident wavevectors (\vec{k}^{in}) of rays and phases Φ on each surface are known. The endpoints of the rays are calculated based on the following equations:

$$\vec{k}_{tr}^{out} = \nabla\Phi + \vec{k}_{tr}^{in} \quad (3.3a)$$

$$\vec{S}_e = \vec{S}_0 + l \frac{\vec{k}_{tr}^{out}}{|\vec{k}_{tr}^{out}|} \quad (3.3b)$$

In metasurface synthesis, the origins (\vec{S}_0) on the input plane and endpoints (\vec{S}_e) of rays on the detector surface are known. The goal is to find the phases (Φ) of one/more surfaces by using the reverse of Generalized Snell's Law.

$$\vec{k}^{out} = |\vec{k}| \frac{\vec{S}_e - \vec{S}_0}{l} \quad (3.4a)$$

$$d\Phi = \int (\vec{k}_{tr}^{out} - \vec{k}_{tr}^{in}) \cdot d\vec{l} \quad (3.4b)$$

Eq. (3.4b) represents a line integral on a specific plane. The total derivative $d\Phi$ must exist for real metasurface. Even if it does not exist, one can find an approximate solution for $d\Phi$ in many cases. After analyzing the system, one can find the deviation from the desired response.

3.3 Generalized Snell's Law in Cylindrical Coordinate System

In most optical systems, the light primarily propagates in a specific direction. This is called the system's optical axis. Metasurfaces are flat surfaces which are mostly perpendicular to the optical axis. This configuration makes the cylindrical coordinate system an ideal choice for analyzing such a system. The optical axis is chosen along the z-axis and \hat{z} represents the unit vector in this direction. \hat{r} and $\hat{\phi}$ are the unit vectors to represent any vector in the transverse plane. In Figure 3.3 a ray propagates from surface I to surface II. The distance between the surface is z.

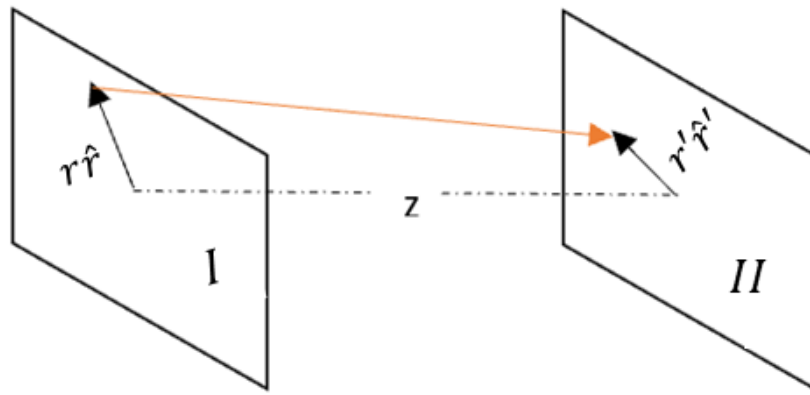


Figure 3.3. Ray propagation in cylindrical coordinate system

From Figure 2.3. we can write

$$\vec{S}_0 = r \hat{r} + 0 \hat{z}$$

$$\text{and, } \vec{S}_e = r' \hat{r} + z \hat{z}$$

$$\text{so, } \vec{S}_e - \vec{S}_0 = \Delta\vec{r} + z \hat{z} \text{ with } \Delta\vec{r} = (r' - r)\hat{r}$$

$$\text{and, } l = \sqrt{\Delta r^2 + z^2}$$

Using Eq. (3.4b)

$$\frac{\vec{k}^{out}}{k_0} = \frac{\vec{S}_e - \vec{S}_0}{l}$$

$$\text{or, } \frac{\vec{k}_{tr}^{out} + k_z^{out} \hat{z}}{k_0} = \frac{\Delta\vec{r} + z \hat{z}}{l}$$

Equating the component along unit vectors

$$l = z \frac{k_0}{k_z^{out}} = z \frac{k_0}{\sqrt{k_0^2 - (k_{tr}^{out})^2}} \quad (3.5a)$$

$$\text{and, } \Delta\vec{r} = z \frac{\vec{k}_{tr}^{out}}{\sqrt{k_0^2 - (k_{tr}^{out})^2}} \quad (3.5b)$$

Applying Generalized Snell's law, one can obtain \vec{k}_{tr}^{out} from the transverse component of the input wavevector \vec{k}_{tr}^{in} and phase gradient $\Delta\Phi$ on the surface as in Eq. (3.3a).

3.4 Example of Phase-only Metasurface

One of the commonly used metasurfaces is metalens. Metalenses focus the optical beam to a point on the optical axis. This point is called the focal point. Functionally, metalenses are similar to refractive optical lenses, which have been used for a long time. Refractive lenses are built by curving glass into specific shapes (flat, convex, or concave). Metalenses offer flat and compact solutions for optical focusing. Spherical aberration-free metalenses implement the hyperbolic phase profile.

$$\Phi(r) = -k_0 [\sqrt{r^2 + f^2} - f] \quad (3.6)$$

and, so

$$\nabla\Phi = -k_0 \frac{r}{\sqrt{r^2 + f^2}} \hat{r}$$

Here, f is the focal length of the lens. For the normally incident input beam ($\vec{k}_{tr}^{in} = 0$), the output transverse wavevector component can be found using Eq. (3. a).

$$\vec{k}_{tr}^{out} = \Delta\Phi + 0 = -k_0 \frac{r}{\sqrt{r^2 + f^2}} \hat{r}$$

Now using Eq. one can show that

$$\begin{aligned} \Delta\vec{r} &= f \frac{\vec{k}_{tr}^{out}}{\sqrt{k_0^2 - (k_{tr}^{out})^2}} \\ &= -f \frac{k_0 \frac{r}{\sqrt{r^2 + f^2}} \hat{r}}{\sqrt{k_0^2 - \left(k_0 \frac{r}{\sqrt{r^2 + f^2}}\right)^2}} \hat{r} \\ &= -r \hat{r} \end{aligned}$$

$$\text{So, } \vec{r}' = \vec{r} + \Delta\vec{r} = 0$$

This indicates that all the rays will be focused on the focal point ($r = 0, z = f$). For the input beam with a non-zero incident angle, we can carry on a similar analysis. Let's assume, the incident beam makes an angle θ_{inc} with the optical axis. The transverse component of the incident wavevector can then be written as $\vec{k}_{tr}^{in} = k_0 \sin\theta_{inc} \hat{r}_{inc}$, where \hat{r}_{inc} is the unit vector along the transverse component of the incident wavevector. Again using Eq. (3. a) we can calculate \vec{k}_{tr}^{out} .

$$\vec{k}_{tr}^{out} = \Delta\Phi + k_0 \sin\theta_{inc} \hat{r}_{inc} = -k_0 \frac{r}{\sqrt{r^2 + f^2}} \hat{r} + k_0 \sin\theta_{inc} \hat{r}_{inc} \quad (3.7)$$

In this case, ray deflection $\Delta\vec{r}$ for arbitrary \vec{r} is very difficult to compute analytically. However, for the center of the beam ($r = 0$) the calculation is still doable, and we obtain the center deflection $\Delta\vec{r}_c$.

$$\begin{aligned}
\Delta \vec{r}_c &= f \frac{\vec{k}_{tr}^{out}}{\sqrt{k_0^2 - (k_{tr}^{out})^2}} \\
&= f \frac{k_0 \sin \theta_{inc}}{\sqrt{k_0^2 - (k_0 \sin \theta_{inc})^2}} \hat{r}_{inc} \\
&= f \tan \theta_{inc} \hat{r}_{inc}
\end{aligned} \tag{3.8}$$

Eq. 3.8 shows that the center of the beam will be deflected by $f \tan \theta_{inc}$ along \hat{r}_{inc} . This is expected and can be obtained easily using the simple geometric argument. For bulk refractive lenses, the center of the beam goes through at least two refractions, and its deflection may not exactly match the result of Eq. (8).

3.5 Physical Design of Metasurface

Metasurface modifies the propagation of light by applying a phase gradient. Using geometric optics, one can find the required phase for a specific purpose. In physical design, subwavelength structures are used to apply the required phase. The structures are called meta-unit cells. As phase is 2π periodic, we need a set of meta unit cells that can apply phases from 0 to 2π . Typically, for a single metasurface, the unit cells share some common properties and only one/two dissimilar properties to apply different phases. For example, cylindrical nanopillar unit cells have the same value for the height of the nano-pillar (H), the separation between the nano-pillar (U) and substrate thickness (t) [32]. In this case, different nanopillar diameters create different phase shifts on the incoming light. After obtaining the required phase distribution, one then needs to find the corresponding distribution of nanopillar diameter. The nanopillars are then fabricated on the substrate to create the metasurface.

3.6 Unit Cell Simulation

The layout for simulating a meta unit cell is shown in Figure 3.4. Here, we use a cylindrical nanopillar of height H and diameter D on a thin substrate (thickness t) as the meta unit cell. Typically, the periodic boundary conditions are used to truncate the simulation region in the transverse direction. The total simulation area in the transverse plane is $U \times U$, where U is the separation between the meta unit cells. In the metasurface, U represents the sampling intervals for phase discretization.

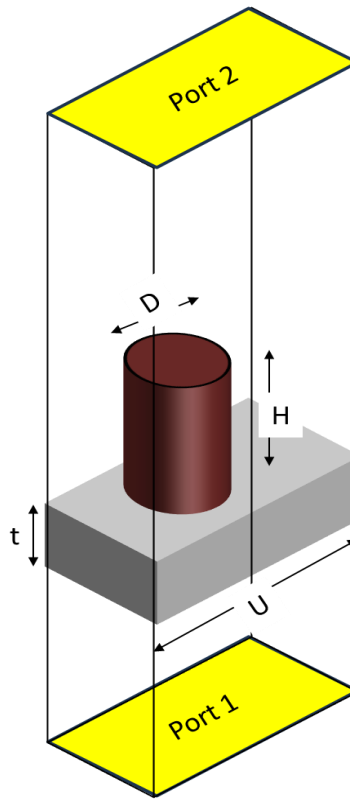


Figure 3.4 Meta unit cell simulation layout

Ports are introduced to excite and absorb light. Here, normally incident plane wave excitation is used with the Floquet periodicity, $k_F = 0$. As $U < \lambda$, only $k_F = 0$ gives the propagating solution. The S_{21} parameters of the unit cells for different nanopillar diameters

are calculated. The obtained phase is biased, as the phase of S_{21} depends on the distance of the input and output plane from the meta unit cell. To get an unbiased estimate, we choose the phase from a particular nano-pillar (NP_s) to be zero. The (relative or) unbiased phases of other nanopillars(NP) are obtained by subtracting obtained S_{21} from the phase of NP_s .

After the materials for nanopillar and substrate are selected, U , H , and t are optimized to obtain phase shift in 0 to 2π range by varying nanopillar diameter D . I will now present a meta-unit cell structure from [33] The meta-unit cell consists of amorphous silicon (a-Si) nanopillar on the quartz substrate. The optimized parameters at the wavelength of $1\mu\text{m}$ are shown in the following table.

Table 3.1. Optimized meta-unit cell parameters at the wavelength of $1\mu\text{m}$

U	350nm
H	450nm
t	170nm

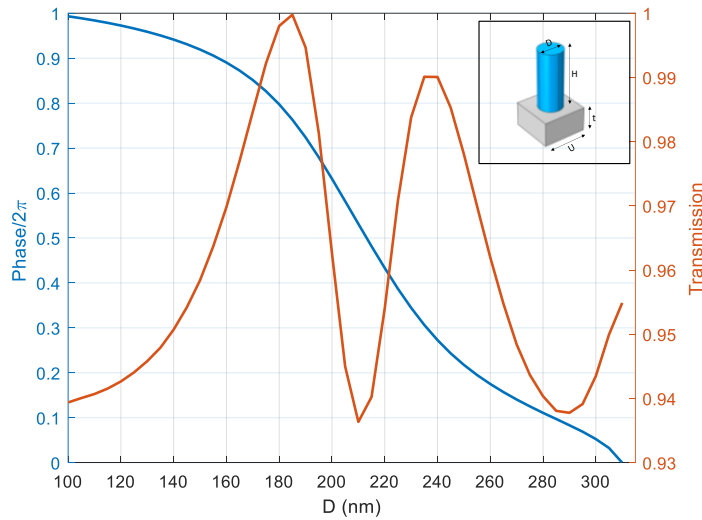


Figure 3.5. Transmission magnitude and phase variations of normally incident beam on meta unit cell structure with the diameter of the unit cell. (The meta unit cell is shown in the inset.)

The meta-unit cell simulation is performed in COMSOL MULTIPHYSICS using Finite Element Method (FEM). The refractive indices of 3.80 and 1.45 are assumed for a-Si and quartz respectively [34]. Plane wave is normally incident from the quartz side and transmission S-parameter S_{21} is calculated. Simulations are done for different nanopillar diameters. The relative transmission phases for different nanopillar diameters are calculated considering the phase from nanopillar of 310nm diameter as reference. Using this platform, we obtained transmission greater than 93% and full 2π phase shift by varying nanopillar diameter from 100nm to 310nm (Figure 3.5). One of the major advantages of such a meta-unit cell is that it is polarization insensitive thanks to its circular symmetry. Such metalens can be fabricated by using Electron beam lithography [35] or by direct patterning on quartz substrate by using deep ultra- violet (DUV) photolithography [36,37].

3.7 Full Wave Simulation of Metasurface

Metasurface analysis using the ray optics/ geometric optics method suffers from the limitations of geometric optics. For example, geometric optics calculation is not valid near the focal point of the lens. Diffractive optics calculation is more applicable in this scenario. In metasurface simulation, geometric optics or diffractive optics do not consider the loss due to the interaction between slightly different meta-unit cells that build the metasurface. In fabricated metasurfaces, the interaction reduces the efficiency of the metasurface. Full wave simulation provides a better estimate of metasurface efficiency. However, the full-wave simulation of metasurfaces poses some challenges.

Usually, metasurfaces are large ($100\lambda \sim 1000\lambda$) 2D structures with a very small height. The phase profile as well as meta-unit cell parameters vary along two transverse directions. As the meta-unit cell separations are small (less than a λ), a typical metasurface

consists of a very large number of meta-unit cells. Full wave simulation (such as FDTD and FEM) of whole metasurfaces requires a very large number of mesh points. That increases the memory requirement for the simulation. Moreover, the output beam is usually desired far away from the metasurfaces (for example, metalens with mm size focal length). This large longitudinal distance in simulation further increases the requirement of computation power. One way to reduce simulation time is to simulate a small propagation region after (and before) the metasurface using the full-wave simulation method. The EM field at the output plane in front of the metasurface is then captured and propagated arbitrarily large distance using the diffractive optics method.

To reduce simulation time further, we can do a simulation of only a row of metasurface. In this case, it is implied that the phase profile is uniform along a direction, say \vec{u}_1 (like a cylindrical lens). One needs to apply Periodic Boundary Conditions (PBC) along the boundaries that are normal to \vec{u}_1 . This will ensure no propagation component along \vec{u}_1 . Along other directions (\hat{z} and $\vec{u}_2 = \vec{z} \times \vec{u}_1$), Perfectly Matched Layer (PML) is applied to absorb any outgoing wave. We call this method the quasi-3D method. Quasi-3D simulation includes interaction between different meta-unit cells in a metasurface, and thus efficiency estimation is more accurate than the diffractive optics-based calculation. The simulation schematic for quasi-3D simulation is shown in Figure 3.6.

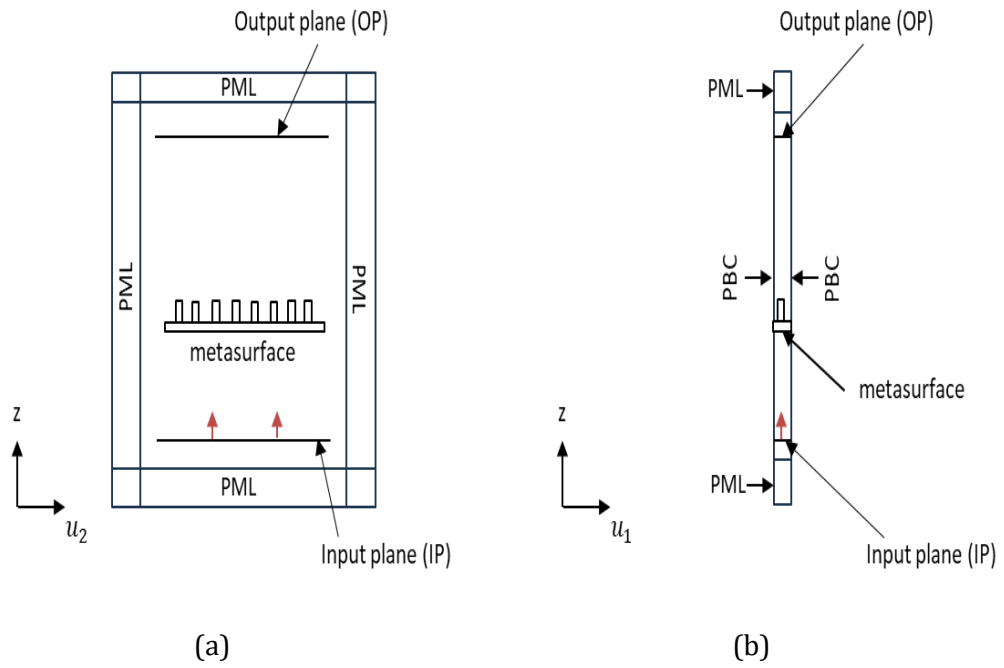


Figure 3.6. Quasi-3D simulation schematic in (a) $u_2 - z$ plane and (b) $u_1 - z$ plane

CHAPTER 4

AOA JITTER TOLERANT OPTICAL RECEIVER

4.1 Background

A simplified conventional receiver system is shown in Figure 4.1. The system consists of an aperture lens with a diameter, a , and focal length, f , which focuses the light on a free space detector. A conventional system is designed in a way so that the detector captures the normally incident beam at the focal plane ($AoA, \theta_{inc} = 0^\circ$). In a real system, there is always some AoA fluctuation. Non-zero AoA leads to beam walk-off in two directions orthogonal to the optical axis. In the cartesian system, the z-axis is usually considered as the optical axis. In this case, AoA deviation leads to beam walk-offs δ_x and δ_y along the x and y directions respectively. The beam walk-off on the detector leads to degradation of the received power on the detector and, consequently, higher BER. The level of degradation depends on the focused beam size, detector area, and focal length of the aperture lens.

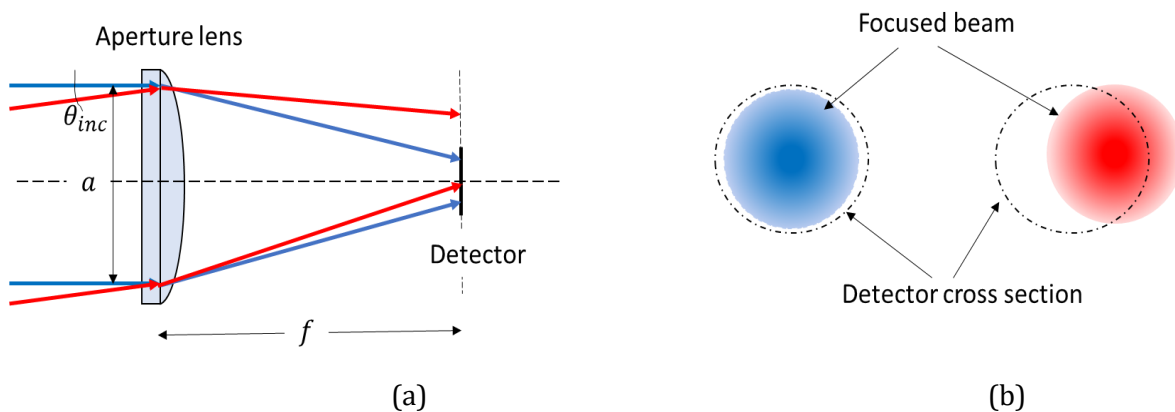


Figure 4.1. (a) Conventional receiver with normal (blue ray) and oblique incident beam (red ray). (b) Beam walk-off on detector plane in the conventional receiver for normal (blue) and oblique (red) incident beam.

The power reduction due to beam walk-off can be quantified by the performance degradation factor, K . We define $K = P_d/P_{av}$, where P_d is the power received by the (finite-sized) detector and P_{av} is the total power available at the (infinite) detector plane. If the focusing optics is lossless, we get $P_{av} = P_{rec}$ where P_{rec} is the total optical power received by the receiver aperture. The performance degradation factor (K) can be obtained from the focused beam intensity distribution on the detector plane, $I_d(x, y)$

$$K = \frac{\iint_{A_{lum}} I_d(x-\delta_x, y-\delta_y) dx dy}{\iint_{A_{beam}} I_d(x, y) dx dy} \quad (4.1)$$

Here, the integration in the numerator is carried out only on the detector area, (A_{lum}) which is illuminated by the focused beam (as shown in Figure 4.2a), and the integration in the denominator is carried over the full focused beam area (A_{beam}). With no beam walk-off ($\delta_x = \delta_y = 0$), K attains its maximum value, K_0 . K_0 depends on detector size (A_{det}). $K_0 = 1$ implies an ideal case when the full focused beam is captured by the detector. Due to rotational symmetry, K is only a function of radial beam walk-off $\delta = \sqrt{\delta_x^2 + \delta_y^2}$.

We can evaluate the effect of beam walk-off on K in an ideal system. In this system, a Gaussian beam with beam diameter $2w_0$ is incident on a lossless aberration-free aperture lens with focal length f . The focused beam is another Gaussian beam with the beam diameter $2w = \frac{4\lambda f}{\pi(2w_0)} = \frac{4\lambda}{\pi} \times f - number$ [38]. We chose $I_d(x, y) = \frac{2}{\pi w^2} e^{-\frac{2(x^2+y^2)}{w^2}}$ so that the integration in the denominator of Eq. 4.1 always remains 1 and we only need to run numerical integration over the finite area of A_{lum} . The variation of K with radial beam walk-off (δ) for different $f - number$ of the aperture lens is shown in Figure 3.2b with detector

radius (r_d) of $20\mu\text{m}$. Note that for an $f/30$ aperture lens, the beam size is larger than the detector area and hence, K is less than 1 even for normal incidence.

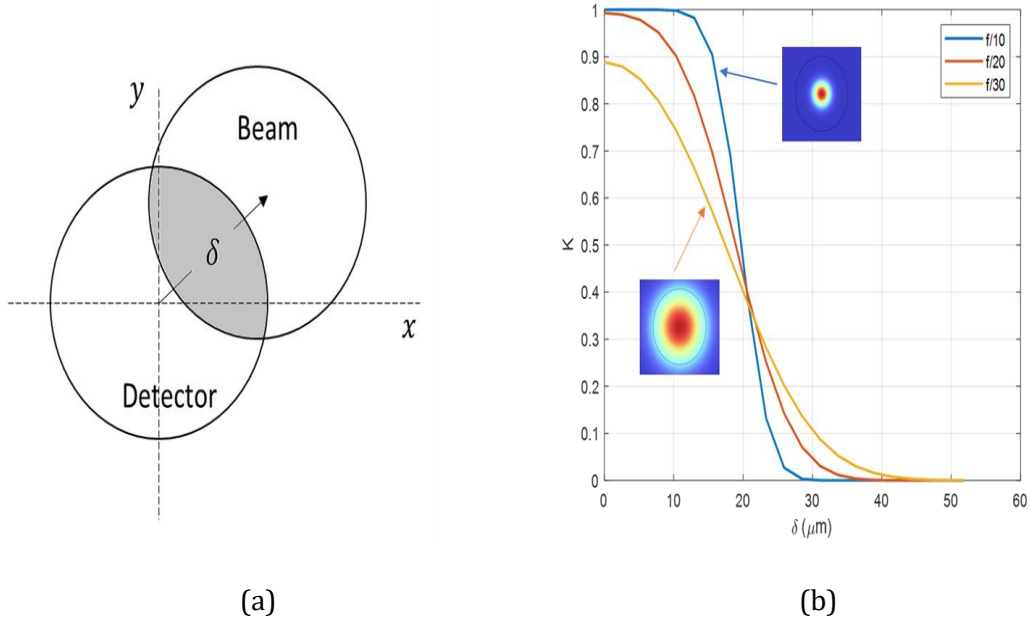


Figure 4.2. (a) Detector and beam overlap area (grey shaded region) for calculation of power degradation factor, K , (b) K versus beam walk-off (δ) for an ideal system with a detector radius of $20\mu\text{m}$. The insets show beam profile (a.u.) for the $f/10$ and the $f/30$ system where a solid black circle represents the detector boundary.

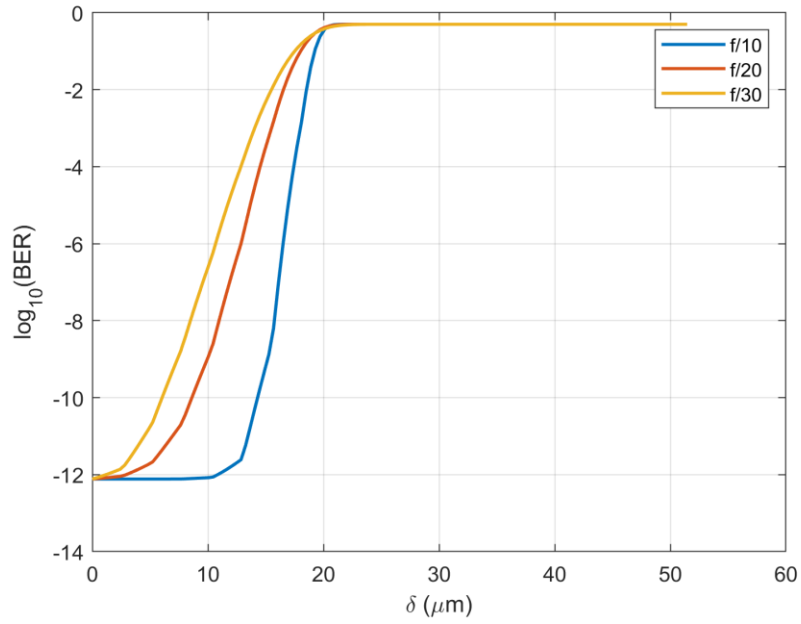
It is obvious from Figure 4.2b that K has a smoother variation with radial beam walk-off for the system with a larger focused beam size. This implies that the effect of AoA fluctuation jitter is lower for such a system. A large, focused beam is possible in two ways, either for a long focal length or for a very small aperture size. In the first case, the receiver becomes very large and can violate SWAP constraints. In the second case, the captured power from the transmitting beam will be very low, which increases the power budget of the optical link. It is possible to optimize beam size so that the link fulfills specific performance criteria. BER, average BER, and power penalty are some of the performance criteria of optical links. In our ideal system, we can evaluate these criteria as follows. The incident optical signal on the

detector generates photocurrent that depends on detector responsivity, R , and optical power on the detector, $P_d = P_{rec} K$ (assuming $P_{rec} = P_{av}$). The photocurrent also contains a noise component, n , which arises due to several factors, such as shot noise, dark current, thermal noise, APD excess noise factor, flicker noise, etc. The overall photocurrent can be modeled as $i_d = P_{rec} K R + n$. Here, for proof of concept, we focus on on-off keying (OOK) modulation where the received signal can have two power levels 0 and P_{rec} for the bit 0 and 1 respectively. The BER can be calculated using the following formula. (derivation is shown in Appendix)

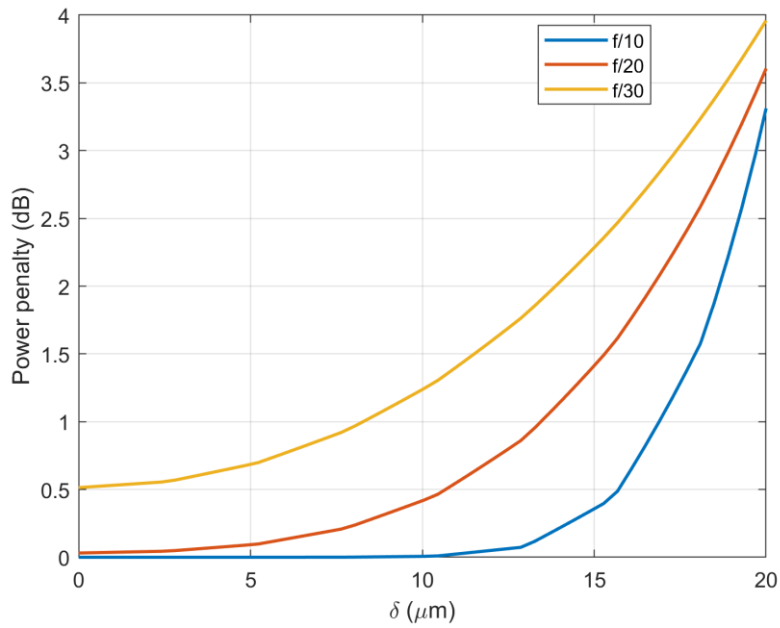
$$BER(K) = \frac{1}{2} \left[Q\left(\frac{P_{Th}}{\sigma_n}\right) + Q\left(\frac{P_{rec}K - P_{Th}}{\sigma_n}\right) \right] \quad (4.2)$$

Here, $Q(\cdot)$ represents the Q-function and σ_n is the variance of the detector noise, n . Although only OOK is presented here, the results can be extended to coherent communication systems or systems using block codes. Since all modulation formats benefit from increased power efficiency, we anticipate that reducing the jitter will improve the BER and maximum reach of alternative modulation schemes.

In our calculation, we assume the responsivity of the photodiode is $R = 1$. The decision level threshold is assumed fixed at $P_{Th} = \frac{P_{rec}}{2}$, where P_{rec} is the received power for the normally incident beam on the aperture lens in the receiver system. The fixed P_{Th} approximation is justified as it is not possible to dynamically adjust P_{Th} with the fast variation of AoA. The BER variation with K is shown in Figure 4.3a. For the calculation, we assume that in system design P_{rec} is selected so that $BER \approx 10^{-12}$ at $AoA = 0$ assuming full beam power is available on the detector $P_d = P_{rec}$.



(a)



(b)

Figure 4.3. (a) BER and (b) power penalty for an ideal conventional system with a detector radius of $20\mu\text{m}$

In a realistic system, the beam wandering, and phase front distortions will cause stochastic variations in the received power and angle of arrival. We can calculate the

statistical average of the BER as $E[BER] = \int_0^\infty p(\delta) BER(\delta) d\delta$. Here, $p(\delta)$ is the probability density function of radial beam walk-off. Without turbulence, beam walk-offs along two orthogonal directions are assumed to be independent random variables with the Gaussian distribution of variance σ and mean zero. Then $p(\delta)$ turns out to be Rayleigh distribution $p(\delta) = \frac{\delta}{\sigma^2} e^{-\frac{\delta^2}{2\sigma^2}}$ [6]. By using a suitable pdf, we can also include the effect of turbulence in the proposed system.

When the performance degradation factor is less than 1, excess power is needed to maintain the same BER as $K = 1$. Such ‘Power penalty’ can be calculated from K as *Power penalty (dB)* = $10 \log_{10} K$. The power penalty for a conventional system with respect to variation of beam walk-off is also shown in Fig 4.3b.

Static optimization to reduce the AoA jitter involves finding a suitable $f - number$ that results in the desired $E[BER]$ when the system’s jitter variance is known beforehand. We can then fix the system’s aperture with the receiver length constraints. The system is built with optimized parameters and deployed. However, jitter variance can change with time, which requires re-optimization. One can also perform dynamic optimization, in which the transmitting beam size is varied dynamically to keep $E[BER]$ at the desired level. This method necessitates feedback from the receiver to the transmitter. Other dynamic methods include dynamically controlling the fast-steering mirror [10] or tuning the focal length of the aperture lens [3].

In this work, we propose a new solution to reduce the effect of AoA jitter. We present a static solution to capture large AoA (and hence large beam walk-off) with a high-performance factor. As a result, $E[BER]$ will not degrade drastically for systems with large

jitter variance. The proposed solution involves integrating metalens in the conventional receiver, which is lightweight and works within SWAP constraints. The solution does not require feedback from the receiver, any additional processing power, or mechanical movements like dynamic methods of reducing the impact of AoA jitter.

4.2 Proposed System

Our proposed system consists of an aperture lens and a detector like a conventional receiver. We added a metalens in the system as shown in Figure 4.4(a). The objective of the metalens is to correct the phase front of the beam so that the focal point remains the same for different AoA values. Since the phase front of the beam varies as the beam propagates in the receiver system, the metalens must be customized based on their specific location in the receiver.

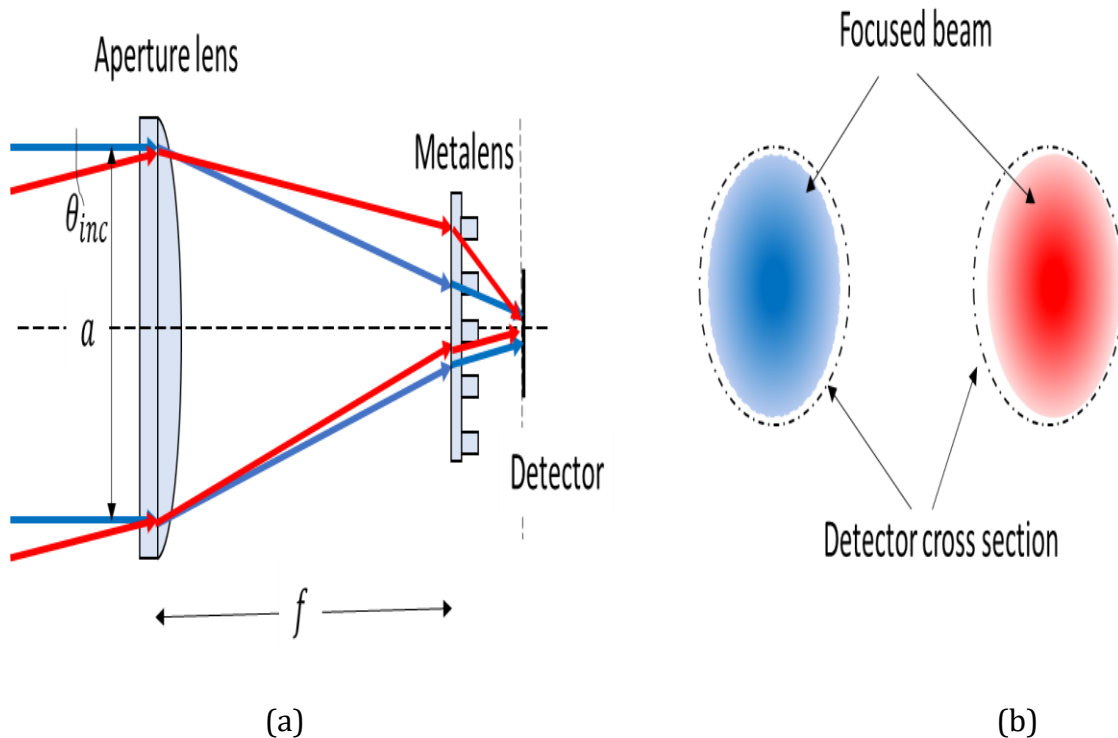


Figure 4.4. (a) Proposed receiver with the normal (blue) and oblique incident beam (red). (b) Beam walk-off on detector plane in the proposed receiver for normal (blue) and oblique (red) incident beam

In our proposed system, the metalens is added to the focal plane of the aperture lens to alleviate the beam walk-off issue due to AoA fluctuation, as shown in Figure 4.4a. The metalens redirects and focuses the incident beam with different AoA to the center of the detector. To do that, the phase profile of the metalens should be $\phi(r) = b r^2$. Here, r represents the radial coordinate of the points on the plane of metalens. The parameter b is the phase constant that needs to be optimized such that the beam with $\theta_{inc} = \theta_{opt}$ will be focused on the center of the detector. We chose θ_{opt} to be the maximum expected AoA of the communication link $\theta_{opt} = \theta_m$. In this way, beam walk-off for all the angles $-\theta_m < \theta_{inc} < \theta_m$ will be improved compared to the conventional receiver system. The coefficient b can also be obtained analytically by applying the Generalized Snell's law which is shown in the appendix.

Our chosen phase profile is quadratic, which can lead to spherical aberration for large metalens. But, as we place the metalens near the focus of the aperture lens, the required metalens diameter is small ($\sim \mu m$). So, we expect that the effect of spherical aberration from metalens will be negligible. However, the aberration from the aperture lens needs to be considered, as it can change the shape of the focused beam after the metalens.

4.3 Result and Analysis

As proof of concept, here we designed and analyzed a system consisting of an aperture lens with aperture diameter $a = 10mm$ and focal length $f = 100mm$ ($f/10$ system). We used a commercially available lens model in OpticStudio to perform ray optics-based and physical optics-based simulations. (The simulation model of the lens also incorporates the effects of aberration from aperture lens). The operating wavelength is $1\mu m$. Initially, we designed the system for $\theta_{opt} = 1mrad$. From ray-based simulation, optimized phase constant, b is found

to be $-6188.907 \text{ rad/mm}^2$. 'Binary 2' surface feature in OpticStudio is used to simulate metalens. The ray diagrams for the conventional receiver and our proposed receiver are shown in Figure 4.5a and Figure 4.5b respectively.

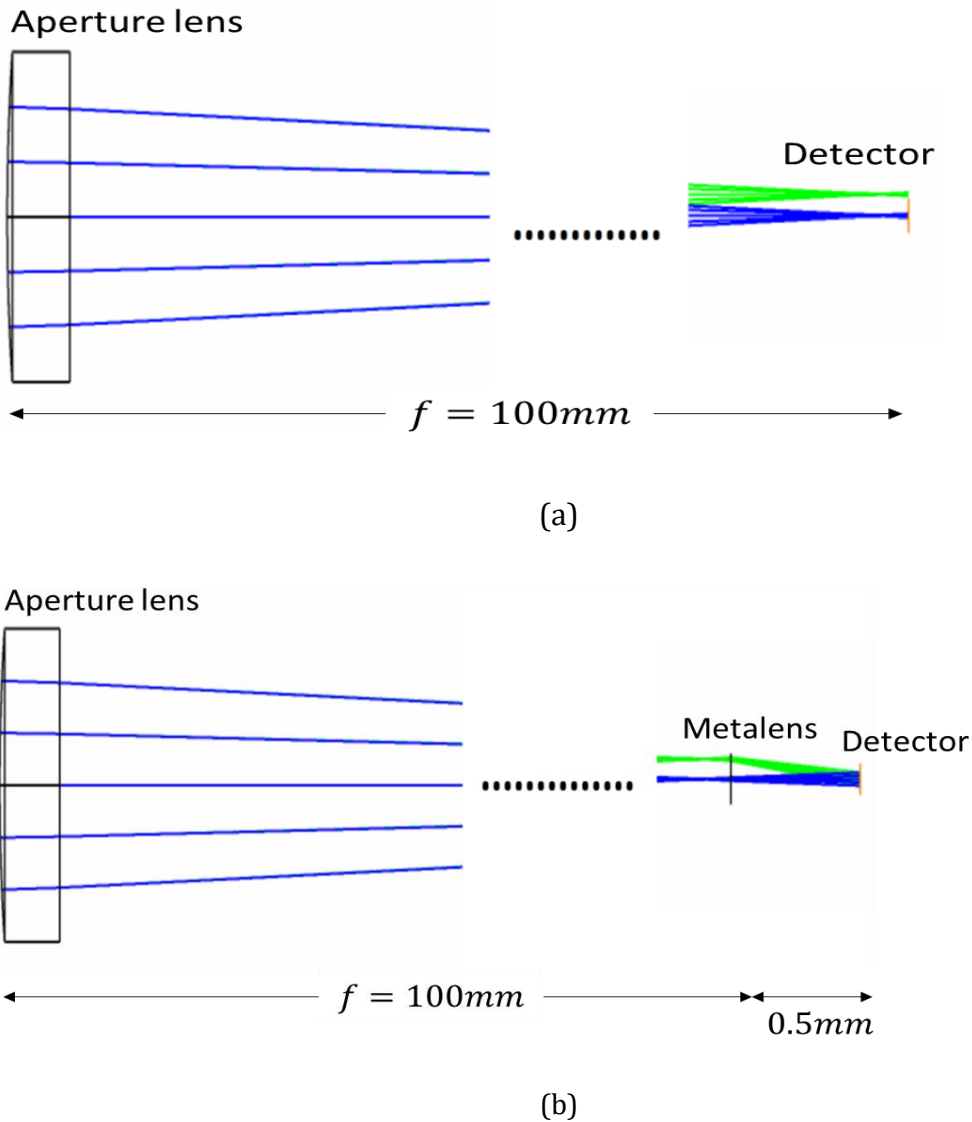


Figure 4.5. Ray diagram for the conventional receiver (a) and ray diagram for the proposed receiver (b). Blue rays indicate $AOA=0rad$ and green-ray indicates $AoA = 1mrad$.

We calculated the beam walk-off for AoA ranging from 0 to $1mrad$. It is observed that our designed system can significantly reduce the beam walk-off for a large range of AoA

(Figure 4.6). Due to reduced beam walk-off, the captured optical power for fixed radius optical detector is improved.

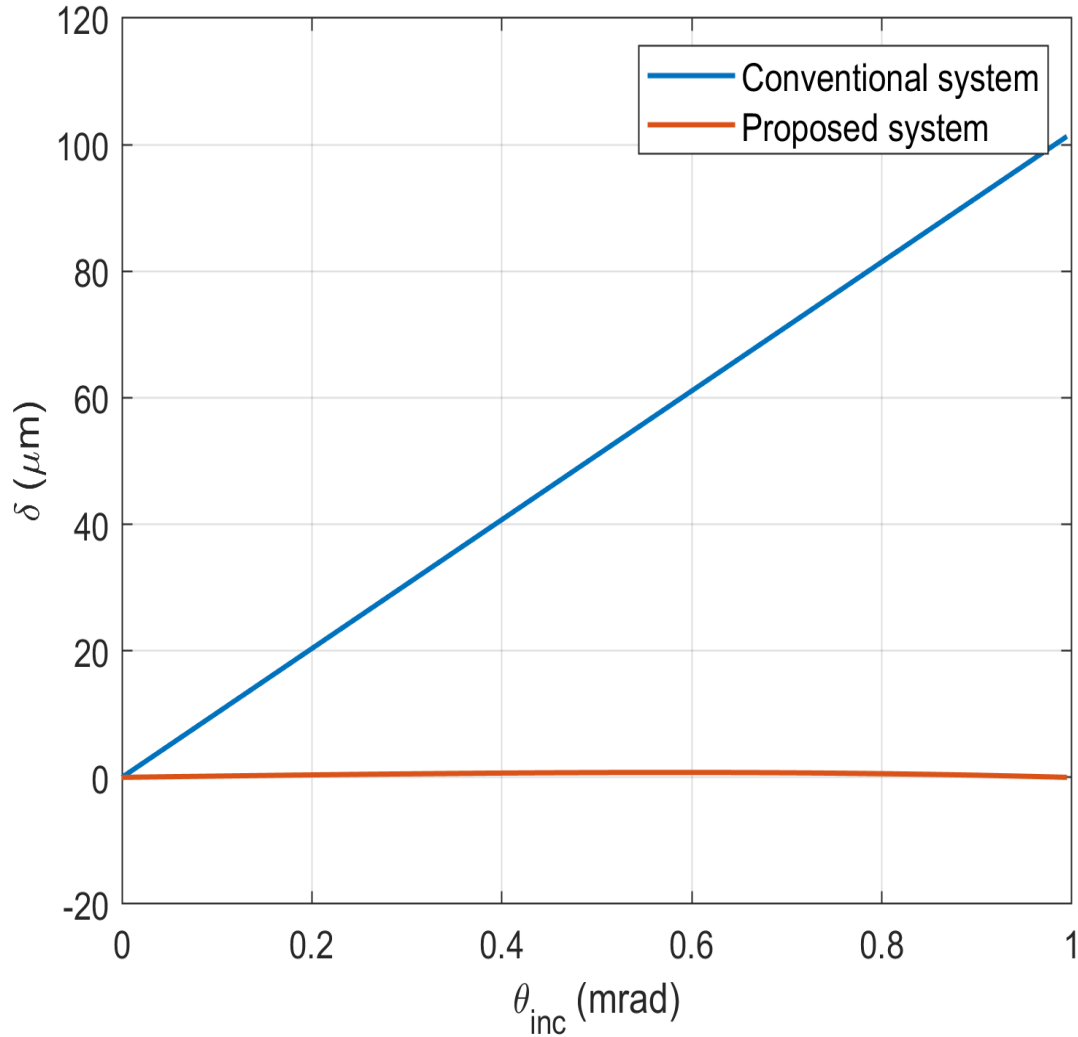


Figure 4.6. Beam walk-off (δ) for different AoA (θ_{inc})

Physical Optics Propagation (POP) simulation is carried out to calculate the power degradation factor and the associated power penalty with AoA for a detector with a radius of $20\mu\text{m}$. The results are shown in Figure 4.7a and Figure 4.7b respectively. For POP simulation, a Gaussian beam with a beam waist, $w_0 = 5\text{mm}$ (beam diameter, $2w_0 = 10\text{mm}$) is used as the input beam. [With other input beam shapes, we expect a slight variation in

beam width due to the diffraction effect. However, the results will follow a similar trend].

Using K for each AoA, we calculated the BER for both conventional and proposed systems.

As shown in Figure 4.7c,

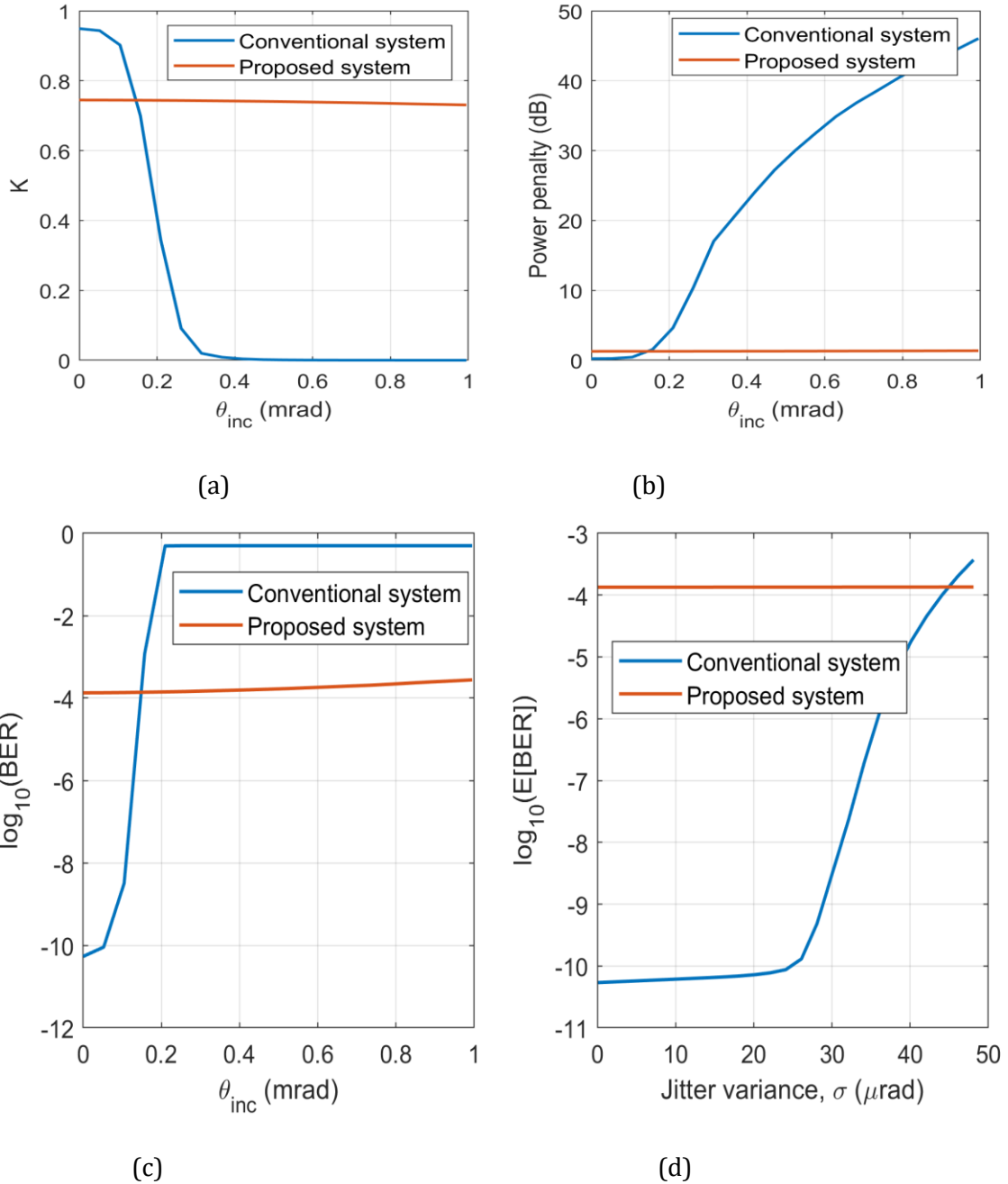


Figure 4.7. (a) Power degradation factor (K) (b) power penalty and (c) BER variation with AoA (θ_{inc}) for the conventional and the proposed receiver with detector radius $20\mu\text{m}$. (d) $E[\text{BER}]$ for different jitter variance.

The BER for the conventional system degrades for larger AoA but it remains almost the same for our proposed system. Here, the BER for our system is worse than the conventional system at normal incidence for the same P_{rec} , as the beam expands before reaching the detector (Figure 4.5b). A bigger spot size on the focus of the aperture lens will help reduce the spot size on the detector and will thus improve the BER. By simple calculation, we can show that when our system's f -number is greater than 19.8, the detector with radius $20\mu m$ can capture the full beam, leading to $K = 1$ for normal incidence and thus minimum BER. The average BER, $E[BER]$ for different jitter variance σ is presented in Figure 4.7d. Relatively constant BER with AoA leads to almost fixed $E[BER]$ for our proposed system whereas for the conventional system, $E[BER]$ significantly degrades for variance greater than $25\mu rad$. Both the conventional and the proposed systems perform better with larger detector area. The result verifies that our proposed system shows robust performance in the presence of AoA fluctuation. In our design, phase constant b is optimized for a fixed location along the optical axis with the metalens surface perfectly normal to the optical axis. After b is optimized, an offset in the metalens position along the optical axis (z-axis) can change beam walk-off and hence can change K . Due to angular invariance in phase profile, tilt around the optical axis cannot alter K , but tilt along other axes will degrade K . In Appendix A, we discuss the effect of small tilt and displacement of metalens.

4.4 Full Wave Simulation

Full wave simulation (FWS) of the full receiver system requires high computational resources. To make the simulation manageable, we divide our system into several sub-systems as shown in Figure 4.8 and only the region near the metalens is simulated by the full wave simulation using Finite Element Method (FEM). First, the physical optics propagation

(POP) based on the diffraction theory is carried out in OpticStudio to find the beam profile (shown in Figure 4.8) at the focal plane of the aperture lens. We use TE polarization with the beam deflected along the y direction ($\phi = \frac{\pi}{2}$). The physical optics method provides a fast estimation of the scattered field with a good level of accuracy if the wavelength of the incident wave is significantly smaller than the radius of curvature of the lens. Only E_x polarization is considered for simulation simplification.

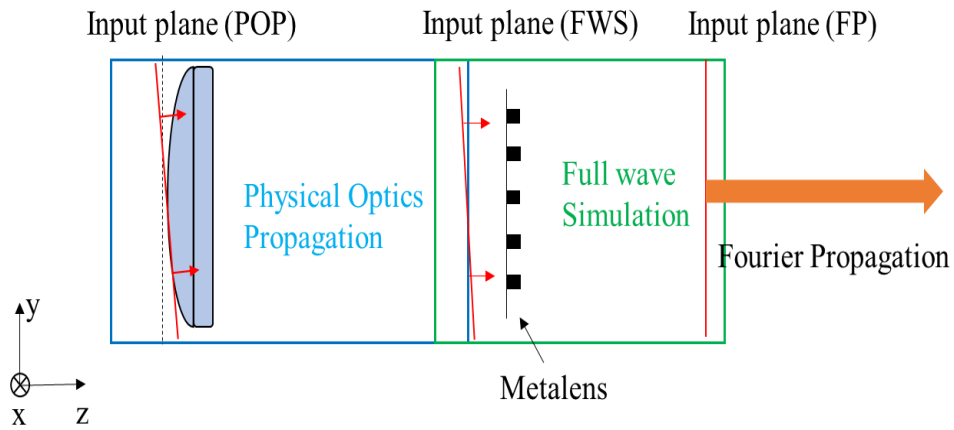


Figure 4.8. Simulation block diagram

From the 2D beam profile (shown in Figure 4.9), the beam along $x = 0$ cross section is selected as the input reference for the full wave simulation (FWS). It is assumed that the beam is uniform along the x direction (quasi-2D beam profile). In quasi-3D simulation, we design only a single row of metalens based on the $x = 0$ cross-sectional phase pattern ($\phi(y) = by^2$). Along the x direction, we used periodic boundary conditions so the input beam and metalens rows are both invariant along the x direction. The width along the x direction is set as the period of metalens U . As $U < \lambda$, only 0th-order(normal) propagation exists along the x direction. The desired phase $\phi(y)$ is sampled with separation U and nanopillars with diameter giving the sampled phases are placed in the appropriate location. The input field

profile is excited by defining magnetic surface current density ($\vec{M}_s = \vec{n} \times \vec{E}$). Perfectly Matched Layer (PML) is applied in all the other boundaries to eliminate unwanted backscattering to the simulation domain. The beam profile on a plane in front of metalens is captured and used as the input field for the final Fourier optics-based (FP) calculation.

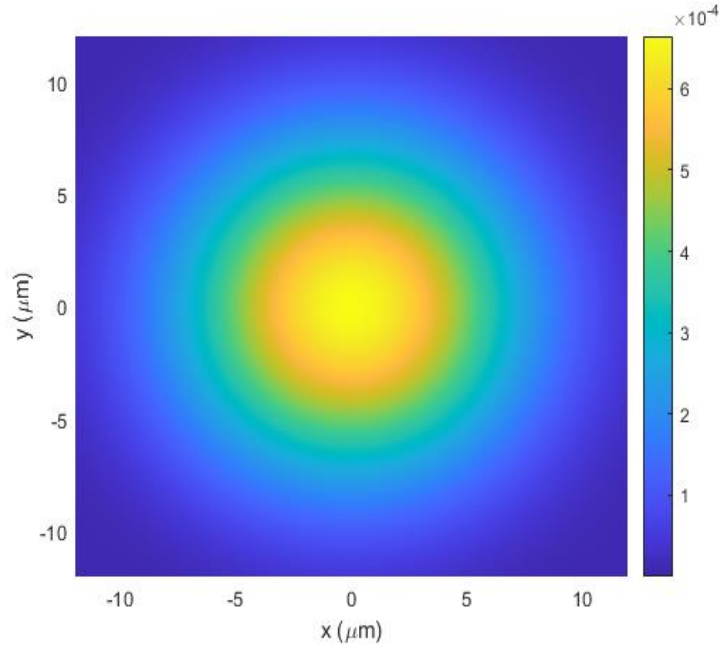


Figure 4.9. Beam profile from POP calculation

Beam evolutions after metalens for three different incident angles (0mrad, 0.5mrad, 1mrad) are shown in Figure 4.10a-c. In all cases, the beams go through the detector sitting 500 μm away from the metalens plane. We estimate K as 0.82, 0.79, and 0.80 for 0mrad, 0.5mrad, and 1mrad respectively. Physical Optics simulation gives a K value of around 0.74. The discrepancy arises for several reasons. The POP simulation assumes metalens is 100% efficient. Quasi-3D full wave simulation includes metalens scattering losses for 1D aperiodic arrangement of varying nanopillar diameter. In a real lens, nanopillar diameter would be varied along the 2D plane and the efficiency will be lower than the one obtained in quasi-3D simulation. With 80% efficiency for 1D phase variation, we estimate an efficiency of 64% for

2D phase profile variation. Although conventional lenses can be more efficient (>95%), we cannot achieve similar functionality as metalens. This degradation in power by metalens can be compensated by increasing the system's power budget.

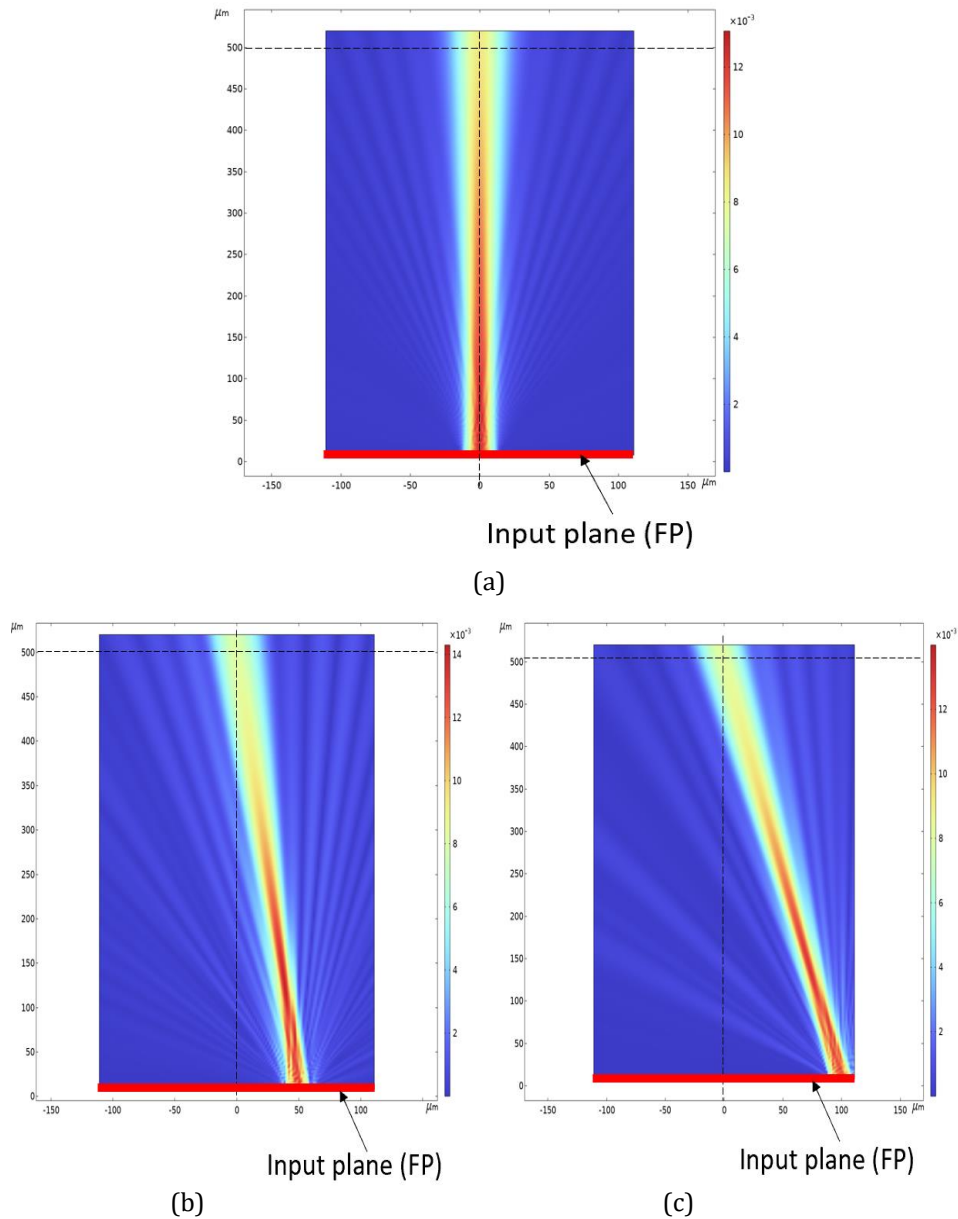


Figure 4.10. (a) Simulation block diagram. Fourier propagation results for $\theta_{inc} = 0$ (b), $\theta_{inc} = 0.5\text{mrad}$ (c), and $\theta_{inc} = 1\text{mrad}$ (d). Field values are in arbitrary units (a.u.)

Here, we realized the desired quadratic phase profile by placing nanopillar with corresponding diameter in appropriate location. Due to fabrication inaccuracy, the nanopillar diameter can vary from the ideal case. This will change the phase imparted by the metalens. By using uniform diameter inaccuracy distribution, the simulation result shows that rms phase variation can be 0.05 and 0.01 for max diameter variation of 1nm and 5nm respectively. Further study is needed based on actual fabrication inaccuracy distribution.

4.5 Region of operation

In our proposed system, the phase coefficient b is calculated so that the beam walk-off for $\theta_{inc} = \theta_{opt}$ will be zero. For other $\theta_{inc} < \theta_{opt}$, the beam walk-off (δ) is not exactly zero. If the beam walk-off is significantly large, the system will not have acceptable performance. To have an idea about how large AoA can be, we designed the system for θ_{opt} up to $5mrad$. We calculated beam walk-off for $\theta < \theta_{opt}$ for each design. The result is presented in Figure 4.11a. The beam walk-off can be significantly high especially when the system is designed for larger θ_{opt} . Large beam walk-off will result in lower K value and wide variation of K for different $\theta < \theta_{opt}$ (Figure 4.11b). This behavior sets a limit on the maximum allowable AoA in our proposed system. The maximum allowable AoA can be defined based on the tolerance level of K for a specific system. We can define the active region of operation θ_{ac} for our proposed system based on the tolerance level of K (K_{tol}) such that

$$\theta_{ac} = \begin{cases} \theta_{opt} & \text{when } \theta_k > \theta_{opt} \\ \theta_k & \text{when } \theta_k < \theta_{opt} \end{cases} \quad (4.3)$$

Here, θ_k is the minimum angle at which $K = K_{tol}$. For the 3D case, the azimuthal part of acceptable AoAs lies within a circle with radius $f \tan \theta_{inc}$. If we select $K_{tol} = 0.5$, θ_{ac} for different θ_{opt} is shown in Figure 4.11c. For comparison, θ_{ac} for a conventional system (the

angle at which $K = 0.5$) is also shown. This analysis shows that we cannot increase θ_{ac} by optimizing b for larger θ_{opt} . But still, our proposed system offers a significant improvement over the conventional system. For $20\mu\text{m}$ detector radius, our proposed system can tolerate AoA of up to 2.5mrad whereas the conventional system can only tolerate less than $200\mu\text{rad}$. For a larger detector radius, our proposed receiver can tolerate even larger AoA variations.

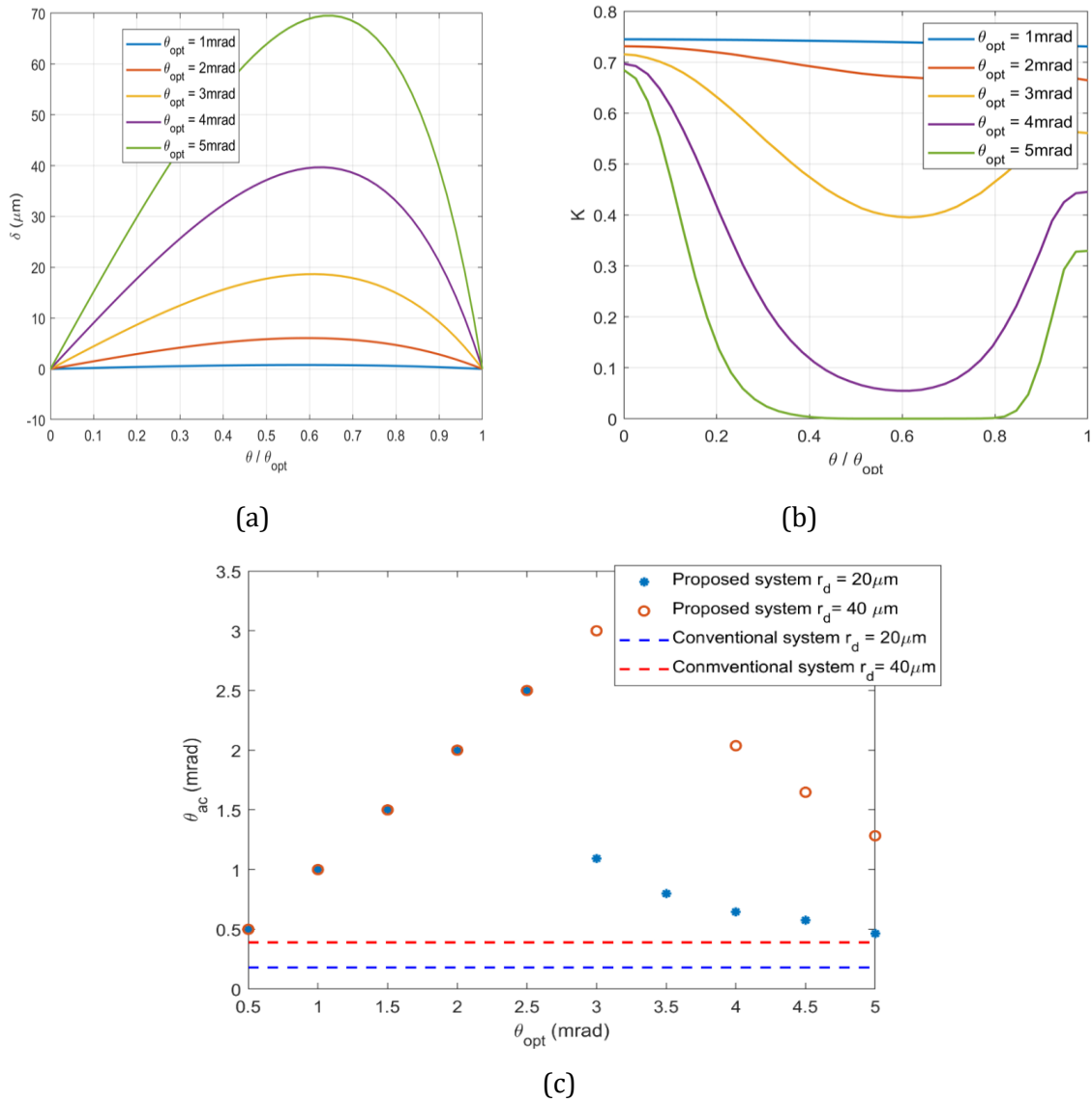


Figure 4.11. (a) Beam walk-off, δ , (b) performance degradation factor, K with different θ/θ_{opt} . (c) The region of operation for different θ_{opt} based on $K_{tol} = 0.5$ criteria.

CHAPTER 5

MULTI-BEAM COMMUNICATION SYSTEM

5.1 Background

Conventional optical receiver in free space optical communication uses a focusing lens to concentrate optical power captured in a large aperture on the small-size photodetector. The receiver accepts only a limited range of AoAs above a threshold performance factor. Using the method presented in Chapter 4, we can estimate the performance factor for different AoAs for any specific receiver system. In Figure 5.1, we presented the calculation for a receiver with a focusing lens of aperture diameter $a = 10\text{mm}$ and focal length $f = 100\text{mm}$.

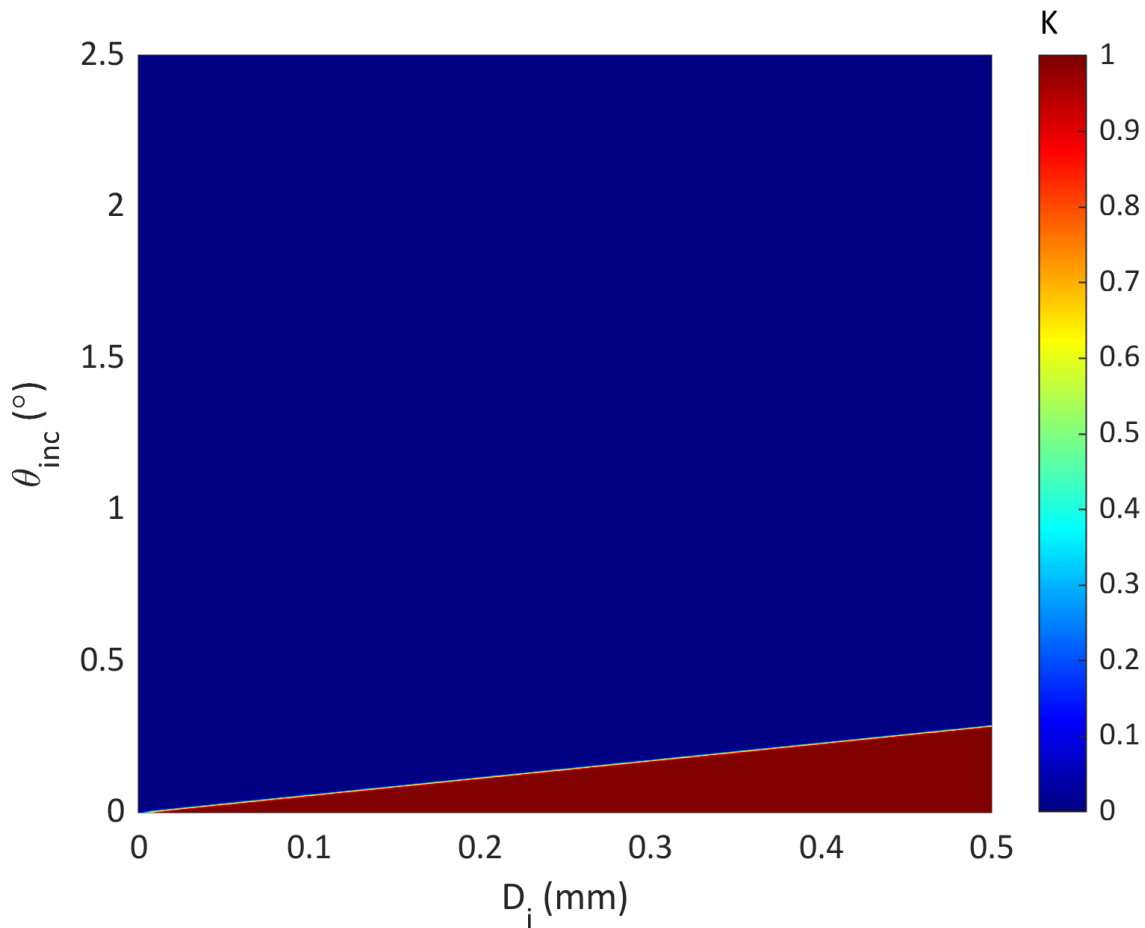


Figure 5.1. Variation of K in a conventional receiver system

We can observe that the receiver system can capture up to 0.056° with a performance factor above 0.5 for a detector diameter $100\mu m$. The receiver cannot capture optical beams from transmitters separated by angles larger than 0.056° from its optical axis. Conventional optical links thus only can establish point-to-point communication.

Multi-beam communication (MBC) where each transceiver can communicate with multiple transceivers has shown great promise in FSO communication. The application of MBC can be classified into two broad categories: spatial diversity and multiplexing. In spatial diversity, the same signal is repeated from multiple transmitters dispersed in space for a single receiver. The redundancy helps to combat the effect of data loss due to turbulence of the transmitting medium or pointing error between the transceivers. When different transmitters send different signals targeting the same receiver, it is called multiplexing. Like fiber optic communication, multiplexing allows communication between multiple nodes without the need for multiple com links. This greatly improves the overall capacity of the link. For example, thanks to WDM, fiber optic communication can reach 1Tb/s capacity. To achieve a similar feat in FSO, one needs a new receiver design that can capture large AoA with a high performance factor. In our work, we propose such a receiver which is built using metalens.

5.2 Proposed System

In Chapter 3, we observe that when an optical beam with non-zero AoA incident on an ideal aberration-free focusing lens, it introduces output transverse wavevector as

$$\vec{k}_{tr}^{out} = -k_0 \frac{r}{\sqrt{r^2+f^2}} \hat{r} + k_0 \sin\theta_{inc} \hat{r}_{inc} \quad (5.1)$$

Here, r varies from 0 to aperture radius a . For center ray ($r = 0$), the transverse wavevector is

$$\vec{k}_{tr}^{out}(r=0) = k_0 \sin\theta_{inc} \hat{r}_{inc}$$

Non-zero θ_{inc} causes the center ray ($r=0$) to deflect by $\Delta\vec{r}_c = f \tan\theta_{inc} \hat{r}_{inc}$. For very large θ_{inc} , the deflection can be significantly large and exceed the radius of a typical high-speed photodetector.

If a second lens at the focal plane adds a correcting wavevector $\vec{k}_{corr}(\Delta\vec{r}_c) = -\vec{k}_{tr}^{out}(r=0)$, then the total wavevector for the center ray will become

$$\vec{k}_2(r=0) = 0 \hat{r} + k_0 \hat{z}$$

Here, the subscript 2 in the wavevector indicates the wavevector is after the second metalens. As a result, the center ray gets parallel to the optical axis. By adding a hyperbolic phase profile (say, with focal length F), we can then redirect the center ray to the center of the detector plane ($r=0, z=f+F$). The correcting phase profile needs to be modified for specific θ_{inc} . However, the focusing phase profile part should be the same for all the θ_{inc} as it works on the parallel beams created by the correcting phase profile.

Based on this idea, we came up with a receiver system consisting of two metalenses (ML1 and ML2) as shown in Figure 5.2. ML1 with diameter a captures the incoming beam and works like the aperture lens of a conventional receiver. As the optical beams with different AoA pass through ML1, they get separated and fall to different locations on the plane of ML2. The distance between ML1 and ML2 is f . The phase profile of ML1 is chosen in a way that the desired AoAs get fully separated on ML2 plane. ML2 focuses all the beams hitting different locations on its surface to the single point (at a distance F) on the optical axis. Finally, a detector with a diameter D_i is placed with the center on the optical axis to capture the focused beam.

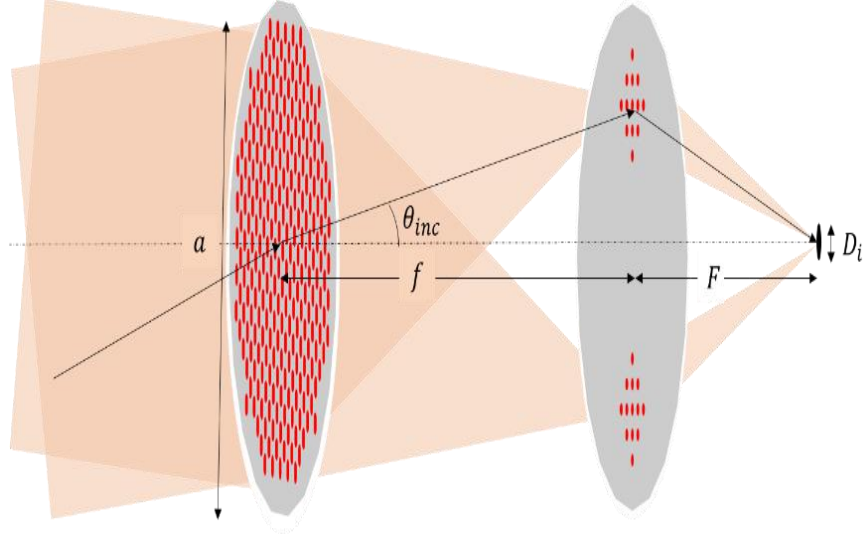


Figure 5.2. Proposed multi-beam receiver architecture

The design of second metalens in the proposed system poses some difficulties. In the FSO system, the aperture diameter needs to be sufficiently large to maximize the amount of captured power from the transmitting beam. When $r \neq 0$, both terms on the RHS of Eq. 5.1 contribute to \vec{k}_{tr}^{out} . As a result, finding a simple closed-form analytical phase profile is very difficult. Moreover, for the ideal lens with a hyperbolic phase profile, the beam at the focus is not well represented by geometric optics calculation. As we are relying on Eq. 4 to synthesize the phase profile, we need to ensure the validity of geometric optics at the location of second metalens. This necessitates the use of a new phase profile for the aperture lens. In our system, we proposed two customized phase profiles for each metalens.

5.3 Phase Profile of The First Metalens (ML1)

The design process starts with the identification of the required phase profile of ML1. We need to satisfy two criteria: spatial separation of different AoAs at the ML2 plane and focus these separated beams on the same plane. A hyperbolic phase profile can perform both functions. But, here, we introduced a phase profile with a tunable parameter, m . The goal is

to focus a normally incident beam with a diameter a to a diameter $a * m$ at the focal plane ($z = f$). Thus, m is a compression factor for $m < 1$. The required phase profile (P_{ML1}) to achieve this goal is obtained by applying Generalized Snell's Laws in a cylindrical coordinate system.

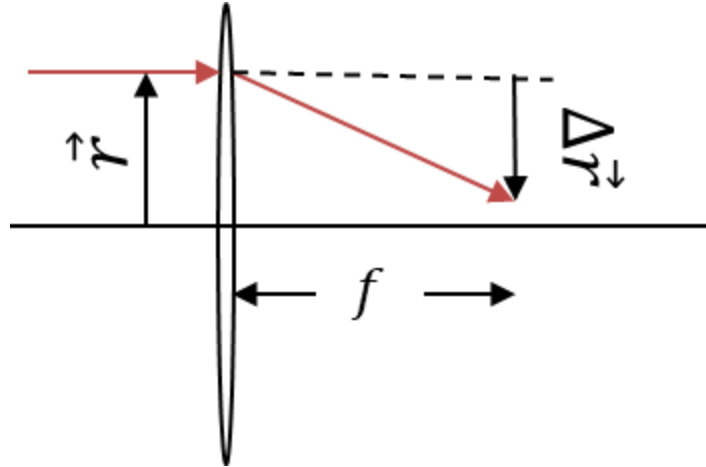


Figure 5.3 Ray diagram for deriving P_{ML1}

Here, we will show how to find a phase profile P_{ML1} for ML1 that compresses a normally incident optical beam by a factor of m . Consider the ray diagram in Figure 5.3. We want

$$\Delta\vec{r} = (1 - m)r\hat{r}$$

However, from Eq. 5. B we know that
$$\Delta\vec{r} = f \frac{\vec{k}_{tr}}{\sqrt{1-k_{tr}^2}}$$

This gives us the following equation

$$(1 - m)r\hat{r} = f \frac{\vec{k}_{ML1}}{\sqrt{k_0^2 - k_{ML1}^2}} \quad (5.2)$$

Here, \vec{k}_{ML1} is the required transverse wavevector of light after leaving ML1. Squaring the magnitude of both sides of Eq. 5.2 we get

$$(1 - m)^2 r^2 = f^2 \frac{k_{ML1}^2}{k_0^2 - k_{ML1}^2}$$

After rearranging and solving, we get $\vec{k}_{ML1} = -k_0 \frac{(1-m)}{\sqrt{(1-m)^2 r^2 + f^2}} \vec{r}$ [where, negative sign is chosen as we want beam compression for $m < 1$]. We know that \vec{k}_{ML1} is related to the desired phase profile of ML1 (P_{ML1}) as $\vec{k}_{ML1} = \nabla P_{ML1}$. Then,

$$P_{ML1} = \int k_{ML1} dr = -k_0 \frac{\sqrt{[f^2 + (1-m)^2 r^2]}}{1-m} + C \quad (5.3)$$

Finally applying the constraints $P_{ML1}(r = 0) = 0$ we get the required phase profile for ML1

$$P_{ML1}(r) = -k_0 \left[\frac{\sqrt{[f^2 + (1-m)^2 r^2]}}{1-m} - f \right] \quad (5.4)$$

Here, k_0 is the free space wavenumber, f is the focal length and r is the radial coordinate of points on ML1. $m = 0$ in Eq. (5.4) corresponds to full-focusing (hyperbolic phase profile) and $m = 1$ corresponds to no-focusing (phase = 0 all around). In other words, by selecting m , we are moving from a “full-focusing lens” to a “non-focusing lens.” In the case of $m = 0$, the focused beam due to non-zero AoA beams cannot be estimated accurately by geometric optics calculation. This creates difficulty in the selection of the phase profile of the ML2. In section 5.5, we will show that this change of behavior can affect the system’s performance significantly. With the phase profile in Eq. 5.4 ML1 applies a transverse wavevector component $\vec{k}_{tr}(\vec{r}, z = 0) = -k_0 \frac{(1-m)r}{\sqrt{f^2 + (1-m)^2 r^2}} \hat{r} + k_0 \sin\theta_{inc} \hat{r}_{inc}$ on the incoming beam. As a result, the center ray will deflect by $\Delta\vec{r}_c = f \tan\theta_{inc} \hat{r}_{inc}$. As a result, beams with different AoAs get separated on its focal plane. For fixed θ_{inc} , the center ray will trace out a circle with a radius $|\Delta\vec{r}_c| = f \tan\theta_{inc}$ when the azimuthal part of the incident angle (ϕ_{inc}) varies which is shown in Figure 5.3.

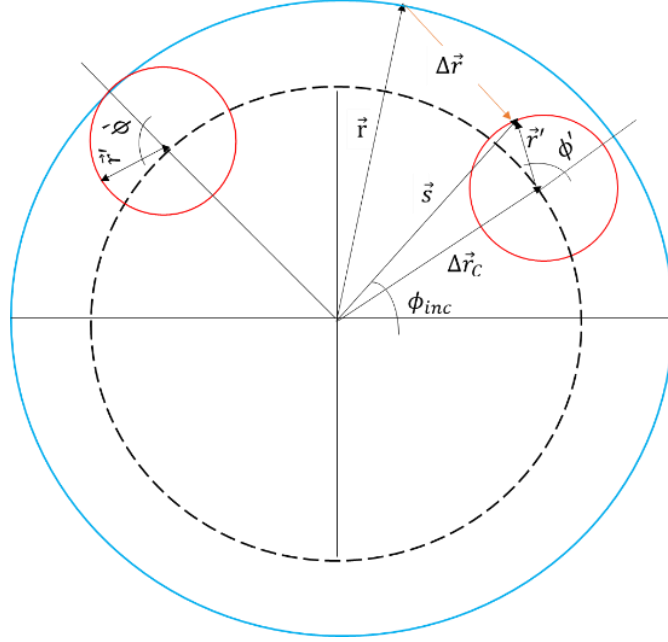


Figure 5.3. Coordinate system for incoming beam (blue) on ML1 and focused beam (red) by ML1

5.4 Phase Profile of The Second Metalens (ML2)

The objective of ML2 is to make the beam parallel to the optical axis and focus the parallel beam on the detector. The phase profile (P_{ML2}) should work on the center ray (as explained before) and for all the portions of the focused beam. Here, we consider a light ray trajectory in the transverse plane as shown in Figure 5.3. The light ray leaving ML1 from $r\hat{r}$ hits ML2 on $r'\hat{r}'$. The origin for the ML2 coordinate system is chosen at $\Delta\vec{r}_c = f \tan\theta_{inc} \hat{r}_{inc}$.

First, we will find a phase profile ($P_{ML2,p}$) that will make all the outgoing beams from ML2 parallel to the optical axis. We make the following two approximations, which will lead to a closed-form solution for $P_{ML2,p}$.

1. $k_z = \sqrt{k_0^2 - k_{tr}^2} \approx k_0 \cos\theta_{inc}$
2. $f \gg (1 - m)a$

The first approximation is justified when the operating AoA is small. For fixed system parameters (f, a) , the second approximation can be justified by choosing a large m value. When these approximations are valid, we obtain a simple relationship between \vec{r}' and r as shown below.

$$\begin{aligned}
\vec{r}' &= \vec{r} + \Delta\vec{r} - \Delta\vec{r}_c \\
&= r\hat{r} + \frac{f}{k_z} \vec{k}_{tr}(\vec{r}) - f \tan \epsilon \hat{r}_{inc} \\
&= r\hat{r} - f \frac{(1-m)r}{\sqrt{(1-m)^2 r^2 + f^2} \cos\theta_{inc}} \hat{r} + f \frac{\sin\theta_{inc}}{\cos\theta_{inc}} \hat{r}_{inc} - f \tan\theta_{inc} \hat{r}_{inc} \quad (\text{using approx. 1}) \\
&= r\hat{r} - \frac{f(1-m)r}{f \cos\theta_{inc}} \hat{r} \quad (\text{using approx. 2}) \\
&= Mr \hat{r}, \text{ With } M = 1 - \frac{1-m}{\cos\theta_{inc}}
\end{aligned}$$

Now we can find the transverse wavevector component $\vec{k}'_{tr}(r', \phi')$ of the focused beam on ML2 in a modified coordinate system on ML2.

$$\begin{aligned}
\vec{k}'_{tr}(r') &= \vec{k}_{tr} \left(r = \frac{r'}{M} \right) \\
&= -k_0 \frac{(1-m)\left(\frac{r'}{M}\right)}{\sqrt{f^2 + (1-m)^2 \left(\frac{r'}{M}\right)^2}} \hat{r}' + k_0 \sin\theta_{inc} \cos\phi' \hat{r}' - k_0 \sin\theta_{inc} \sin\phi' \hat{\phi}' \quad (5.5)
\end{aligned}$$

Finally, the phase profile to make the transmitting beam parallel to the optical axis can be obtained by

$$\begin{aligned}
P_{ML2,p} &= - \int \vec{k}'_{tr} \cdot \hat{r}' dr' + 1/r' \vec{k}'_{tr} \cdot \hat{\phi}' d\phi' . \\
&= k_0 \left[\frac{M}{1-m} \sqrt{f^2 + (1-m)^2 (r'/M)^2} r' - \sin\theta_{inc} \cos\phi' r' \right] \quad (5.6)
\end{aligned}$$

The phase profile in Eq. (5.6) depends on θ_{inc} , but not on absolute ϕ_{inc} . It implies that the ‘azimuth reference direction’ for representing AoA is arbitrary. To accept AoAs with the

same θ_{inc} but different ϕ_{inc} , we need to place $P_{ML2,p}$ in different locations on a circle with radius $f \tan\theta_{inc}$. The receiver can then be rotated around its optical axis to align $P_{ML2,p}$ with the transmitters.

With the addition of the hyperbolic phase profile for focusing, we obtain

$$P_{ML2} = P_{ML2,p} - k_0 \left[\sqrt{s^2 + F^2} \right]$$

$$= k_0 \left[\frac{M}{1-m} \sqrt{f^2 + (1-m)^2 (r'/M)^2} r' - \sin\theta_{inc} \cos\phi' r' \right] - k_0 \left[\sqrt{s^2 + F^2} \right] + const. \quad (5.7)$$

Here, s is the radial distance from the optical axis. The full metalens will have segmented sections where each section will capture specific AoA (as shown in Figure 4.2 and Figure 4.3).

5.5 Result and Analysis

The performance of the proposed system is evaluated based on a receiver architecture with a 1cm clear aperture. The focal length is selected as 5cm, so we can fit it inside a small payload such as a CubeSat. The system parameters are given in Table 1. We will first show the performance of our system for single but wide AoA ($\pm 1^\circ$). Then we will present an analysis for a multi-beam communication system.

Table 5.1. System parameters for an exemplary system

Aperture size, (a)	10mm
Distance between ML1 and ML2, (f)	50mm
Distance between ML2 and detector (F)	20mm
Wavelength	1.55 μ m
AoA (θ_{inc}, ϕ_{inc})	($\pm 1^\circ, 90^\circ$)

First, we calculate the focused beam characteristic by using ray optics (/geometric optics) and physical optics (/diffractive optics) propagation methods. Modeling is performed by using Zemax OpticStudio. Metalenses are implemented using the 'Grid Phase' surface feature. 'Grid Phase' implements a phase map that deflects the incoming beam based on the phase derivative. It works as a lossless implementation of metalens. We mainly use the deviation of the focal point from the optical axis and the size of the focal spot as performance metrics. These two parameters are unified under a single parameter called performance factor, K . When beam walk-off is present or when the beam size gets large or both, K should decrease for a given diameter of the detector centered at the optical axis.

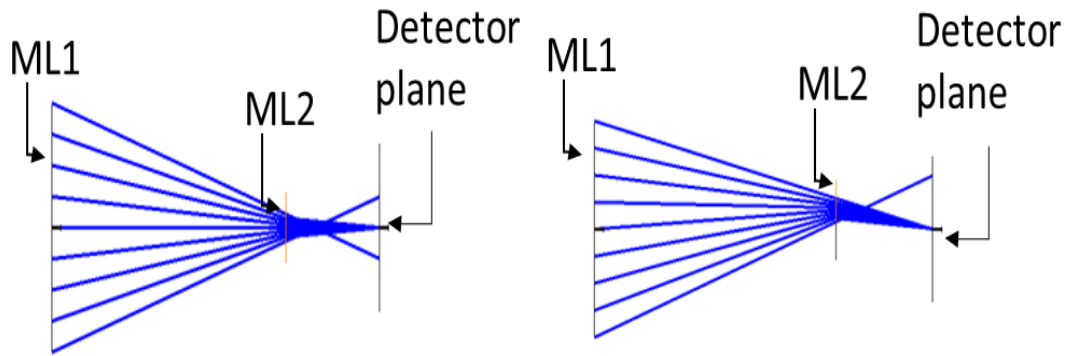


Figure 5.4. Ray diagram of the proof-of-concept system in x-z plane(a) and y-z plane (b).

Ray analysis result (as shown in Figure 5.4a and 5.4b) confirms that the beam with $AoA = 1^\circ$ will get focused to the center of the detector plane. In our simulation, $\phi_{inc} = 90^\circ$ corresponds to the y-axis. As a result, deflection is visible on the y-z plane in the ray diagram. Along the orthogonal x-z plane, there is no deflection. Physical optics calculates the focal spot intensity pattern on the detector plane. The result is shown in Figure 5.5. We observed a 2D focused beam which is ideal to be captured by a 2D detector.

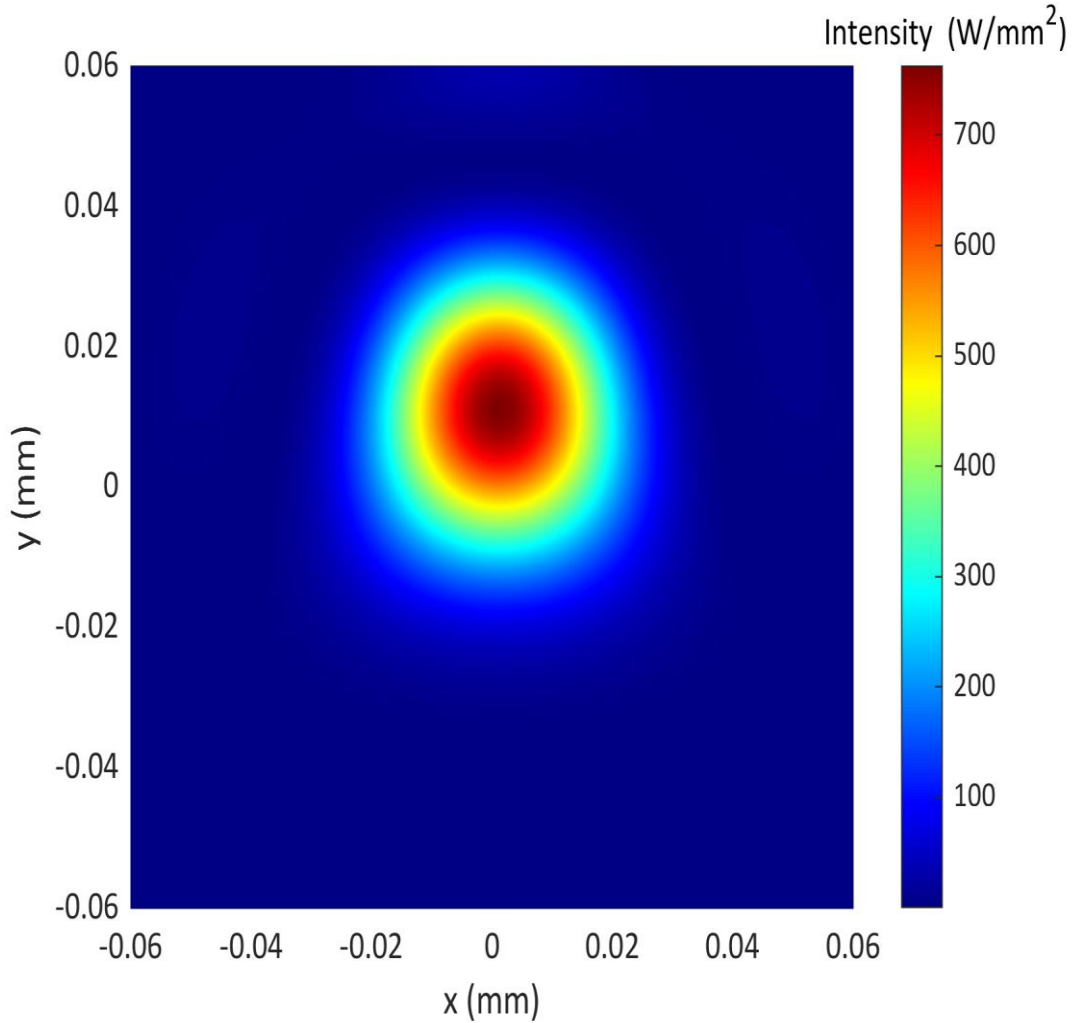


Figure 5.5. Intensity profile on the detector for $m=1/10$

Among many other factors, K depends on detector diameter, D_i . In Figure 5.6 we show the variation of K with detector diameter. The analysis is shown for five different values of m . The performance factor for our system is very high (more than 70% with a $100 \mu\text{m}$ detector diameter) for m values of $1/20$ and above. Due to the high beam walk-off (0.87 mm) coupled with a small beam size ($\sim 15 \mu\text{m}$), the performance factor of the conventional system is close to zero. Also, it is observed that K decreases with the reduction of the value of m . Eventually, K gets too small for $m = 0$. This behavior of the system can be explained by the increasing deviation from the second approximations mentioned before.

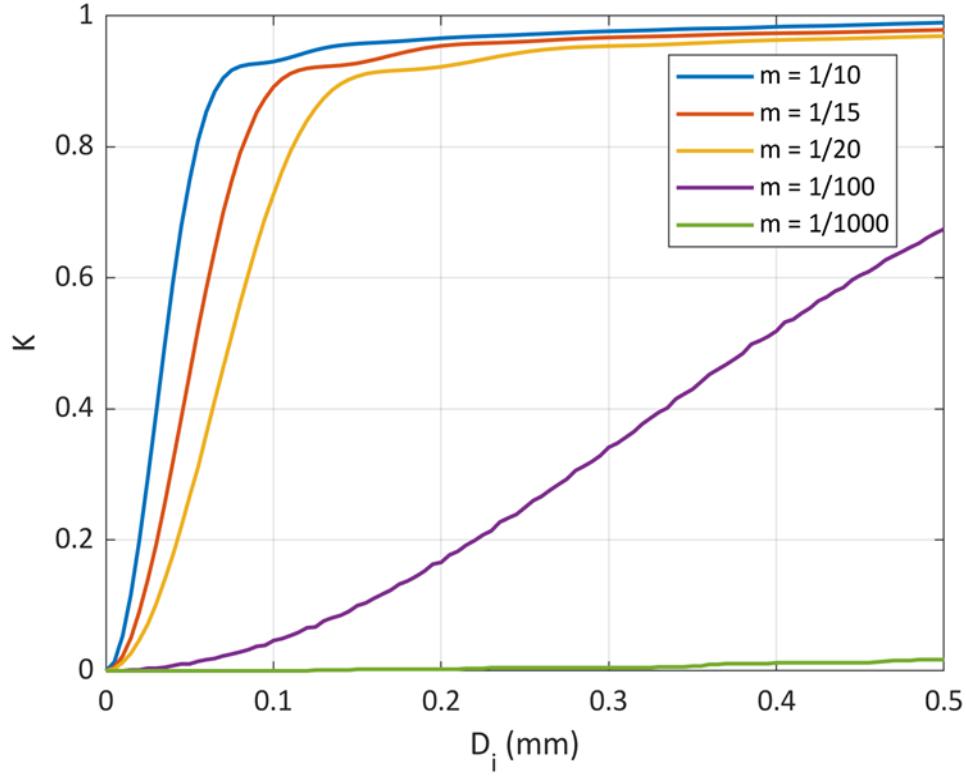


Figure 5.6. Variation of K with detector diameter D_i .

Next, we assess the performance of the proposed system in a three-beam communication link using our receiver system. Here, we designed our system for $\theta_{inc} = 0^\circ, 1^\circ$ and 2° (with $\phi_{inc} = 90^\circ$ for all cases). All the other parameters of the system remain the same as shown in Table 1. We performed similar characterizations above. Although from previous analysis $m = 1/10$ seems to give better performance, we cannot choose this m value in the current scenario. For $m = 1/10$, the focused beam from the 0° and 1° AoAs will overlap on ML2 which leads to ambiguity in implementing the phase profile for ML2. We chose the next better value for m ($m = 1/15$). Ray diagram on the y - z plane shows that all the different AoAs get focused to the center of the detector as shown in Figure 5.7a.

Performance factor with variation of detector diameter for different AoAs is shown in Figure 5.7b. We got $K=0.94, 0.89,$ and 0.69 for $AOA = 0^\circ, 1^\circ$ and 2° respectively.

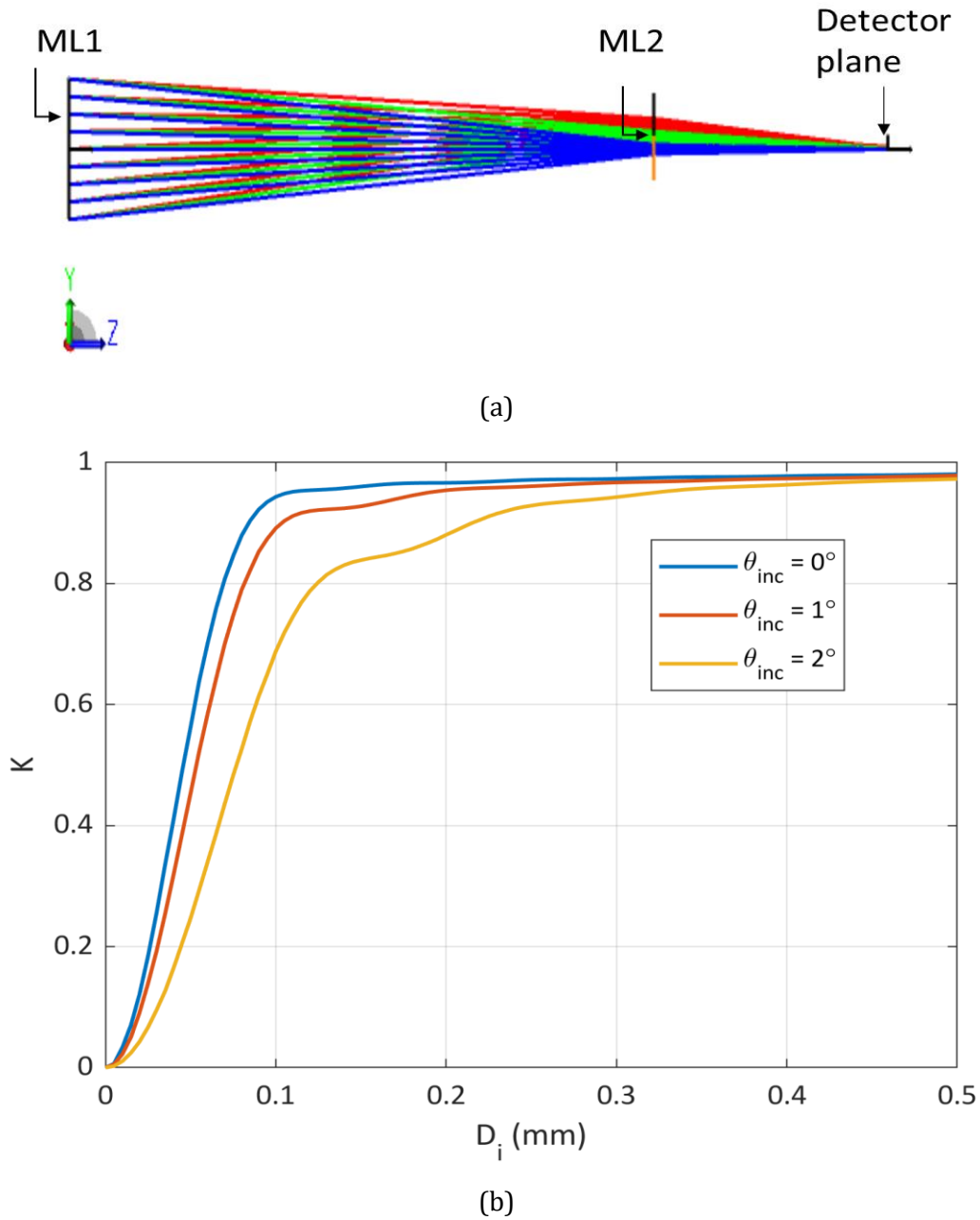


Figure 5.7 (a) Ray diagram for multi-beam optical receiver system for $AOA = 0^\circ$ (blue rays), 1° (green rays) and 2° (orange rays). (b) Performance factor of the same system.

We compare our system with a conventional receiver system having the same aperture of 1cm and focal length $f = 5\text{cm}$. As AoA increases, the beam walk-offs on the detector plane also increase for such a system. With beam walk-off and no correcting element like our proposed system, less power is captured by the detector. Thus, the overall system's K is reduced very fast with increasing AoA. Our system can capture light with larger discrete AoA as shown in Figure 5.8. Figure 5.8 shows that for the designed AoAs, the system shows a very high K value. K degrades as we move away from the designed AoAs. This behavior helps reduce crosstalk between adjacent channels in multi-beam communication.

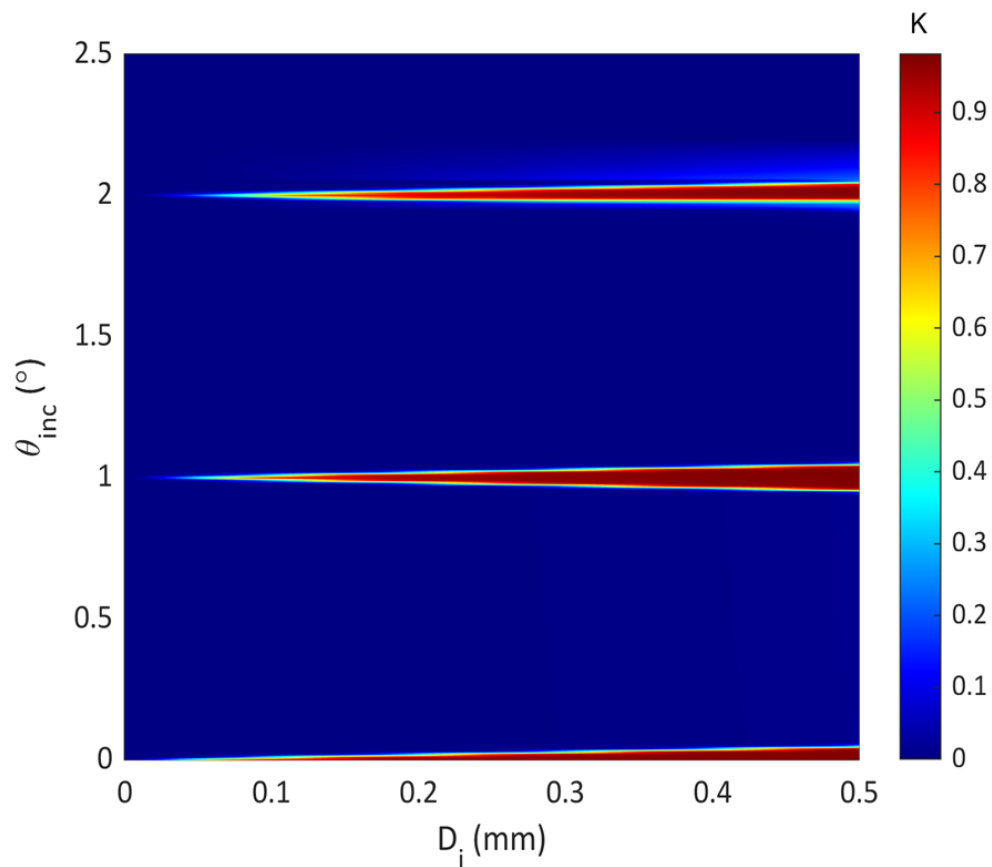


Figure 5.8. Variation of K for the proof-of-concept multi-beam system

In our analysis, we assume that the metalenses are lossless. The losses of metalenses arise from several factors such as the discretization of phase profile, fabrication inaccuracy, etc. The loss of fabricated metalenses also needs to be considered for the performance estimation of the real-world receiver system.

5.6 Meta Unit Cell

Our proof-of-concept multibeam receiver system works at the wavelength of $1.55\mu\text{m}$. We optimized a meta unit cell structure at this wavelength. The meta unit cell is made of crystalline silicon nanopillar on the quartz substrate. The optimized parameters are shown in Table 5.2.

Table 5.2. Optimized meta-unit cell parameters at the wavelength of $1.55\mu\text{m}$

U	680nm
H	840nm
t	340nm

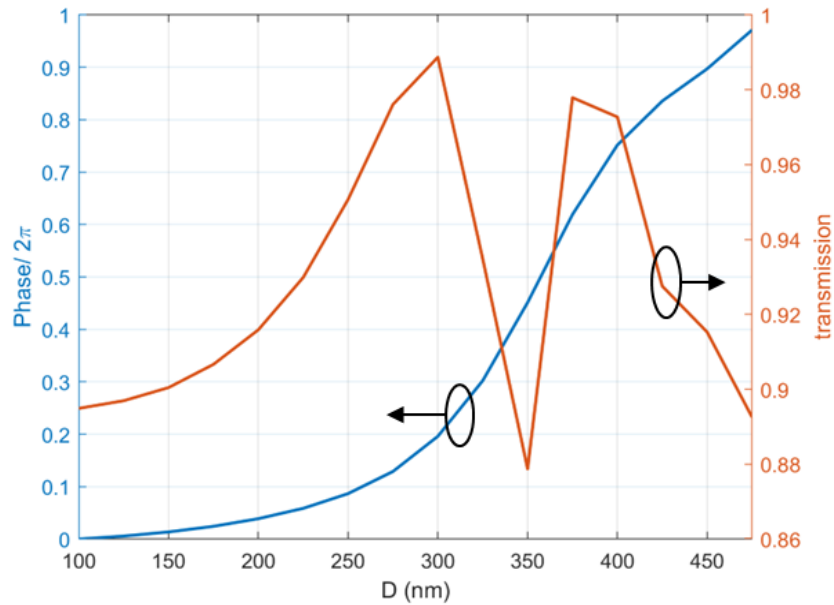


Figure 5.9 Response of optimized meta-unit cell at wavelength $1.55\mu\text{m}$

Using the parameter as shown in Table 5.2, we obtain full $0 - 2\pi$ phase shift by varying nanopillar diameter 100 to 475nm. The response of the unit cell is shown in Figure 5.9.

5.7 Full Wave Simulation of Multi-beam Receiver

We carried out a 3D FDTD simulation by using the Lumerical Software tool to show the efficiency of our system for a small-scale test system. For the test system, we use $a = 40\mu m$, $f = 255\mu m$, $m = 1/2$ and $F = 10\mu m$. Like before, $\phi_{inc} = 90^\circ$ represents the y-axis and we use TE polarization. For each metalens, we first calculated the required phase on a grid with separation U in both x and y directions. Then we placed the unit cells with nanopillars on the grid points. Nanopillar diameters are determined from phase to diameter relationship as shown in Figure 5.9.

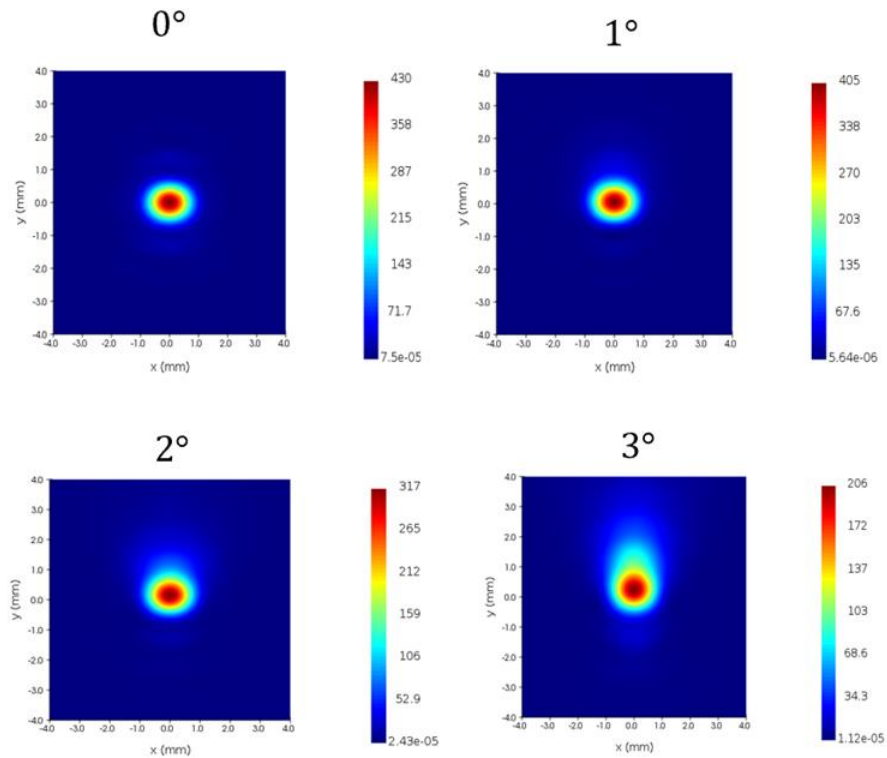


Figure 5.10 FDTD simulation result of optical beam on the detector plane for different AoA

We first simulated a small region surrounding ML1 with a Gaussian beam of radius $20\mu\text{m}$. The field on a plane in front of ML1 is captured for different AoA ($\theta_{inc} = 0^\circ - 3^\circ$ with 1° step). The captured field is propagated to $250\mu\text{m}$ by using the far-field projection method. For the second part of the simulation, the propagated field profile is used to excite light from the source plane at $z = 250\mu\text{m}$. ML2 is placed on $z = 255\mu\text{m}$ and the field on the detector plane $z = 265\mu\text{m}$ is calculated. The intensity profile for different AoAs is shown in Figure 5.10. From the intensity profile, we calculated the radius ($R_{0.5}$) of the detector for which $K = 0.5$. In Figure 5.11, circles are drawn with a radius equal to the corresponding $R_{0.5}$ for each AoA. Also, the beam center (location of peak intensity) for each AoA is shown in Figure 5.11. The efficiency of the full system is obtained as 67.7%, 67.5%, 67.5%, and 65.7% for $AoA = 0^\circ, 1^\circ, 2^\circ$, and 3° respectively. The results confirm the validity of our proposed phase profile in a full 3D system.

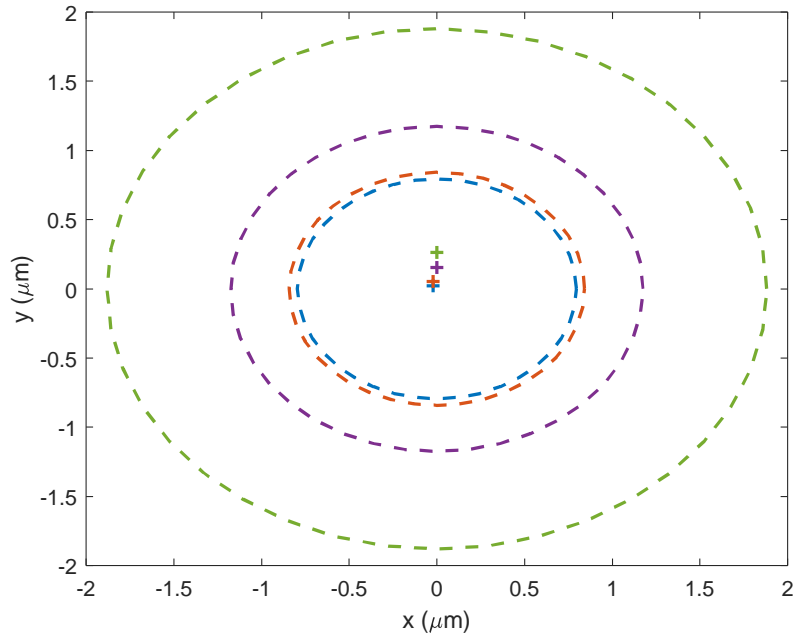


Figure 5.11 A pictorial representation of $R_{0.5}$ (--) with beam center (+) for $AoA = 0^\circ$ (blue), 1° (red), 2° (purple), and 3° (green).

CHAPTER 6

CONCLUSION

In this dissertation, I showed how metalens can be used to build improved receiving optics for free space optical communication. I presented two receiver systems based on metalenses. The first system reduces the impact of the angle of arrival fluctuations jitter. A metalens is introduced in a conventional receiver made with a bulk refractive lens. The phase profile of the metalens is optimized to reduce the beam walk-off on the detector for a large angle of arrival. The receiver provides steady power captured by a small high-speed free space photodetector. As a result, a steady Bit Error Rate is observed for a large angle of arrival jitter variance. The system relaxes the requirements of ultra-fine alignment by the PAT system of inter-satellite free space communication system. Being free of mechanical parts, the system does not interfere with the satellite's control system. In the end, the receiver system increases the probability of long-term uninterrupted data transmission in the presence of an angle of arrival fluctuation.

The second system offers new possibilities for multi-beam optical communication using a single free space detector. The receiver is built with two metalenses. I derived the analytical expression of the phase profiles of the metalenses. The receiver can capture optical beams coming from multiple transmitters dispersed in 3D space simultaneously. It can be optimized for a discrete set of angles of arrival based on the desired network topology. The receiver gets rid of the detector array and the time required to point to each transmitter at a time. In the end, it offers a compact, lightweight solution for multi-beam free space optical communication.

To build the receiver systems, I proposed two metalens unit cells designed for two

different wavelengths ($1\mu\text{m}$ and $1.55\mu\text{m}$). The metalens unit cells are optimized using Finite Difference Time domain (FDTD) and Finite Element Method (FEM) simulation. A strategy for full-wave simulation of the metalens system is discussed. I estimated the efficiency of the metalens receiver system using full-wave simulation.

The systems proposed in the thesis work with only free space detectors. As a result, the systems are suitable for Intensity Modulated Direct Detection (IM-DD) communication links. Due to ease of implementation, IM-DD is mostly used in modulation-demodulation format in free space optical communication. However, coherent communication using fiber-coupled photodetector has shown great promise to improve the performance of communication systems in terms of power budget, immunity to amplitude noise, and the possibility of wavelength division multiplexing. Metalens receiver systems with fiber-coupled detectors can be built as a potential extension of the work presented in the thesis.

Metalenses can be regarded as chip versions of bulk optical systems. They create the possibility of building small and compact optical devices for many different uses. In the thesis, I proposed the use of metalenses for free space communication system. The proposed systems add new functionality for the receiving optics. I present guidelines on how to optimize the metalens phase profile for specific purposes. In the future, machine learning methods can be implemented to optimize the metalens phase profile. Optimization can also be performed considering fabrication losses. Similar procedures can be used to build future metalens systems to tackle other problems in free space optical communication.

REFERENCES

1. H. Kaushal and G. Kaddoum, "Optical Communication in Space: Challenges and Mitigation Techniques," *IEEE Communications Surveys Tutorials* **19**, 57–96 (2017).
2. M. A. Khalighi and M. Uysal, "Survey on Free Space Optical Communication: A Communication Theory Perspective," *IEEE Communications Surveys Tutorials* **16**, 2231–2258 (2014).
3. V. V. Mai and H. Kim, "Beam Size Optimization and Adaptation for High-Altitude Airborne Free-Space Optical Communication Systems," *IEEE Photonics Journal* **11**, 1–13 (2019).
4. C.-C. Chen and C. S. Gardner, "Impact of random pointing and tracking errors on the design of coherent and incoherent optical intersatellite communication links," *IEEE Transactions on Communications* **37**, 252–260 (1989).
5. D. K. Borah and D. G. Voelz, "Pointing Error Effects on Free-Space Optical Communication Links in the Presence of Atmospheric Turbulence," *Journal of Lightwave Technology* **27**, 3965–3973 (2009).
6. A. A. Farid and S. Hranilovic, "Outage Capacity Optimization for Free-Space Optical Links With Pointing Errors," *Journal of Lightwave Technology* **25**, 1702–1710 (2007).
7. J. Ma, Y. Jiang, L. Tan, S. Yu, and W. Du, "Influence of beam wander on bit-error rate in a ground-to-satellite laser uplink communication system," *Opt. Lett.*, **OL 33**, 2611–2613 (2008).
8. T. Song, Q. Wang, M.-W. Wu, and P.-Y. Kam, "Performance of laser inter-satellite links with dynamic beam waist adjustment," *Opt. Express* **24**, 11950 (2016).
9. S. Huang and M. Safari, "Free-Space Optical Communication Impaired by Angular Fluctuations," *IEEE Transactions on Wireless Communications* **16**, 7475–7487 (2017).
10. E. Ciaramella, Y. Arimoto, G. Contestabile, M. Presi, A. D'Errico, V. Guarino, and M. Matsumoto, "1.28 terabit/s (32x40 Gbit/s) wdm transmission system for free space optical communications," *IEEE Journal on Selected Areas in Communications* **27**, 1639–1645 (2009).
11. A. M. Brown, D. V. Hahn, D. M. Brown, N. W. Rolander, C.-H. Bair, and J. E. Sluz, "Experimental implementation of fiber optic bundle array wide FOV free space optical communications receiver," *Appl. Opt.* **51**, 3995 (2012).
12. I. U. Zaman and O. Boyraz, "Impact of receiver architecture on small satellite optical link in the presence of pointing jitter," *Appl. Opt.* **59**, 10177 (2020).
13. M. Safari and S. Hranilovic, "Diversity and Multiplexing for Near-Field Atmospheric Optical Communication," *IEEE Transactions on Communications* **61**, 1988–1997 (2013).
14. S. G. Wilson, M. Brandt-Pearce, Q. Cao, and M. Baedke, "Optical repetition MIMO transmission with multipulse PPM," *IEEE Journal on Selected Areas in Communications* **23**, 1901–1910 (2005).
15. J. A. Anguita, M. A. Neifeld, and B. V. Vasic, "Spatial correlation and irradiance statistics in a multiple-beam terrestrial free-space optical communication link," *Appl. Opt.*, **AO 46**, 6561–6571 (2007).
16. A. H. Dorrah and F. Capasso, "Tunable structured light with flat optics," *Science* **376**, eabi6860 (2022).

17. "Metalenses at visible wavelengths: Diffraction-limited focusing and subwavelength resolution imaging," <https://www.science.org/doi/10.1126/science.aaf6644>.
18. M. Veysi, C. Guclu, O. Boyraz, and F. Capolino, "Thin anisotropic metasurfaces for simultaneous light focusing and polarization manipulation," *J. Opt. Soc. Am. B* **32**, 318 (2015).
19. Y. Hu, X. Wang, X. Luo, X. Ou, L. Li, Y. Chen, P. Yang, S. Wang, and H. Duan, "All-dielectric metasurfaces for polarization manipulation: principles and emerging applications," *Nanophotonics* **9**, 3755–3780 (2020).
20. R. Zhao, L. Huang, and Y. Wang, "Recent advances in multi-dimensional metasurfaces holographic technologies," *Photonix* **1**, 20 (2020).
21. G.-Y. Lee, J.-Y. Hong, S. Hwang, S. Moon, H. Kang, S. Jeon, H. Kim, J.-H. Jeong, and B. Lee, "Metasurface eyepiece for augmented reality," *Nat Commun* **9**, 4562 (2018).
22. M. Y. Shalaginov, S. An, F. Yang, P. Su, A. Agarwal, H. Zhang, J. Hu, and T. Gu, "Single-layer Planar Metasurface Lens with $>170^\circ$ Field of View," in *Frontiers in Optics + Laser Science APS/DLS* (OSA, 2019), p. FM4C.1.
23. B. Groever, W. T. Chen, and F. Capasso, "Meta-Lens Doublet in the Visible Region," *Nano Lett.* **17**, 4902–4907 (2017).
24. J. Ma, D. S. Robledo, L. Anzagira, D. Zhang, K. Shahverdi, and S. Masoodian, "A 1.26-inch 40.7 Mega-Pixel Photon-Counting Quanta Image Sensor with 0.35e- Read Noise and 95dB Single-Exposure Dynamic Range," in *Imaging and Applied Optics Congress 2022 (3D, AOA, COSI, ISA, pcAOP)* (Optica Publishing Group, 2022), p. JW5B.4.
25. J. Kovalik, H. Hemmati, and A. Biswas, "10-Gb/s lasercom system for spacecraft," in *Free-Space Laser Communication Technologies XXIV* (SPIE, 2012), Vol. 8246, pp. 86–96.
26. I. U. Zaman, "Omnidirectional Optical Communicator for Cube-Satellite Crosslink: Design and Analysis," UC Irvine (2021).
27. M. Faenzi, G. Minatti, D. González-Ovejero, F. Caminita, E. Martini, C. Della Giovampaola, and S. Maci, "Metasurface Antennas: New Models, Applications and Realizations," *Sci Rep* **9**, 10178 (2019).
28. J. Lee and H. Lee, "Metasurface-Enhanced Antenna System for Terahertz Band Wireless Communications," in *2020 IEEE Wireless Communications and Networking Conference Workshops (WCNCW)* (2020), pp. 1–6.
29. F. C. Okogbaa, Q. Z. Ahmed, F. A. Khan, W. B. Abbas, F. Che, S. A. R. Zaidi, and T. Alade, "Design and Application of Intelligent Reflecting Surface (IRS) for Beyond 5G Wireless Networks: A Review," *Sensors (Basel)* **22**, 2436 (2022).
30. B. Xu, C. Wu, Z. Wei, Y. Fan, and H. Li, "Generating an orbital-angular-momentum beam with a metasurface of gradient reflective phase," *Opt. Mater. Express*, OME **6**, 3940–3945 (2016).
31. N. Yu, P. Genevet, M. A. Kats, F. Aieta, J.-P. Tetienne, F. Capasso, and Z. Gaburro, "Light Propagation with Phase Discontinuities: Generalized Laws of Reflection and Refraction," *Science* **334**, 333–337 (2011).
32. M. Khorasaninejad, A. Y. Zhu, C. Roques-Carmes, W. T. Chen, J. Oh, I. Mishra, R. C. Devlin, and F. Capasso, "Polarization-Insensitive Metalenses at Visible Wavelengths," *Nano Lett.* **16**, 7229–7234 (2016).

33. M. S. Islam, K. Shahverdi, and O. Boyraz, "Metalens integrated receiver to reduce the effect of angle of arrival jitter in free space optical communication," *J. Opt. Soc. Am. B*, JOSAB **40**, 891–899 (2023).
34. T. Hu, Q. Zhong, N. Li, Y. Dong, Y. H. Fu, Z. Xu, D. Li, V. Bliznetsov, K. H. Lai, S. Zhu, Q. Lin, Y. Gu, N. Singh, and D.-L. Kwong, "Demonstration of a-Si metalenses on a 12-inch glass wafer by CMOS-compatible technology," *6* (n.d.).
35. Y. F. Yu, A. Y. Zhu, R. Paniagua-Domínguez, Y. H. Fu, B. Luk'yanchuk, and A. I. Kuznetsov, "High-transmission dielectric metasurface with 2π phase control at visible wavelengths," *Laser & Photonics Reviews* **9**, 412–418 (2015).
36. Q. Zhong, Y. Dong, D. Li, N. Li, T. Hu, Z. Xu, Y. Zhou, K. H. Lai, Y. H. Fu, V. Bliznetsov, H.-J. Lee, W. L. Loh, S. Zhu, Q. Lin, and N. Singh, "Large-area Metalens Directly Patterned on a 12-inch Glass Wafer using Immersion Lithography for Mass Production," in *Optical Fiber Communication Conference (OFC) 2020* (OSA, 2020), p. Th2A.8.
37. L. Zhang, S. Chang, X. Chen, Y. Ding, M. T. Rahman, Y. Duan, M. Stephen, and X. Ni, "High-Efficiency, 80 mm Aperture Metalens Telescope," *Nano Lett.* **23**, 51–57 (2023).
38. S. A. Self, "Focusing of spherical Gaussian beams," *Appl. Opt.*, AO **22**, 658–661 (1983).

APPENDIX A

Effect of Alignment in the AoA Jitter Tolerant Receiver

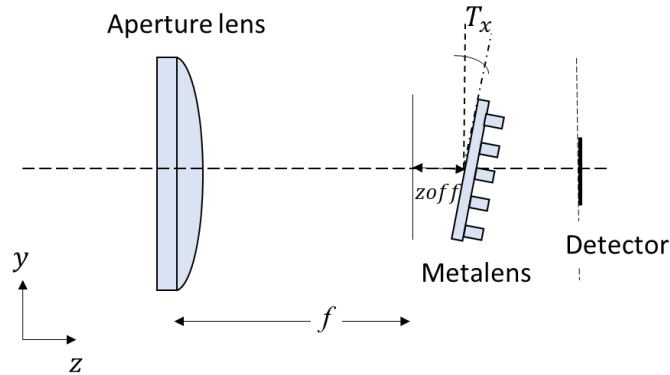


Figure A.1. Definition of offset and tilt.

In our design, the phase constant b is optimized for a fixed location along the optical axis with the metalens surface perfectly normal to the optical axis. After b is optimized, an offset in the metalens position along the optical axis (z) can change beam walk-off and hence changes K . Any tilt along axes other than the propagation axis will degrade K . For example, variation of K with different z_{off} for different tilts around the x -axis, T_x (defined in Figure A.1) is shown in the Figure A.2.

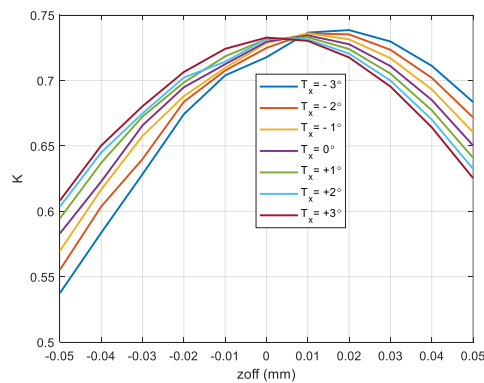


Figure A.2 Effect of tilt around the x-axis

As the system is invariant with respect to tilt about the z-axis (T_z), K does not change for variation of T_z as shown in figure

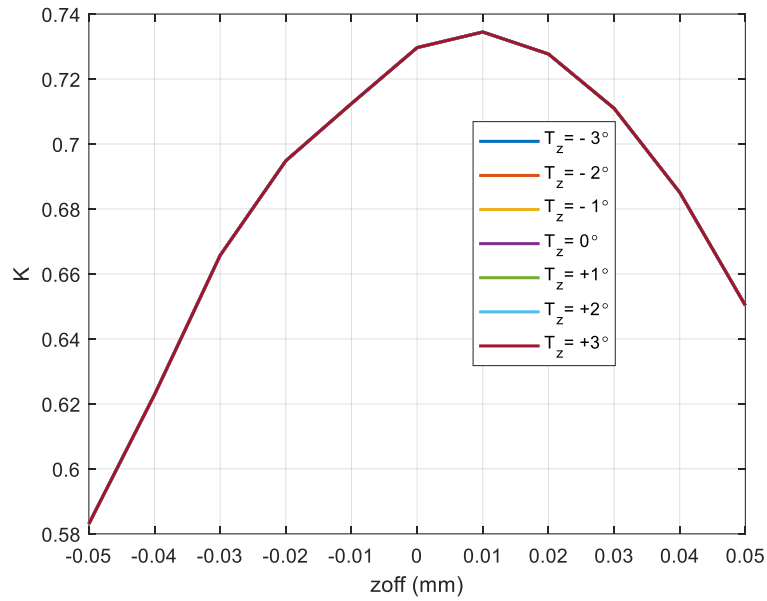


Figure A.3. Effect of tilt around the z-axis